The African Holocene Humid Period in the Tibesti mountains (central Sahara, Chad): Climate reconstruction inferred from fossil diatoms and their oxygen isotope composition

Abdallah Nassour Yacoub, Florence Sylvestre, Abderamane Moussa, Philipp Hoelzmann, Anne Alexandre, Michèle Dinies, Françoise Chalié, Christine Vallet-Coulomb, Christine Paillès, Frank Darius, et al.

The African Holocene Humid Period in the Tibesti mountains (central Sahara, Chad): Climate reconstruction inferred from fossil diatoms and their oxygen isotope composition

Abdallah Nassour Yacoub [a, b, *], Florence Sylvestre [a, b], Abderamane Moussa [b], Philipp Hoelzmann [c], Anne Alexandre [a], Michèle Dinies [c], Françoise Chalié [a], Christine Vallet-Coulomb [a], Christine Paillès [a], Frank Darius [c], Corinne Sonzogni [a], Martine Couapel [a], Jean-Charles Mazur [a], Stefan Kröpelin [d]

[a] Aix-Marseille Université, CNRS, IRD, INRAE, CEREGE, Aix en Provence, France
[b] Université de N'Djamena, Département de Géologie, Laboratoire Hydro-Géosciences et Réservoirs, N'Djamena, Chad
[c] Freie Universität Berlin, Institut für Geographische Wissenschaften, Physische Geographie, Berlin, Germany
[d] Africa Research Unit, Institute of Prehistoric Archaeology, University of Cologne, Germany

ARTICLE INFO

Article history:
Received 13 January 2023
Received in revised form
12 April 2023
Accepted 12 April 2023
Available online xxx

Handling Editor: P Rioual

Keywords:
Oxygen isotopes of diatom silica
Crater palaeolakes
Lake water balance
Diatom-based transfer function
Hydroclimate
ITCZ
Aridification

ABSTRACT

The climate of the African Holocene Humid Period (AHHP) is reconstructed in the Tibesti Volcanic Massif (TVM) in the central Sahara from well-preserved diatomaceous deposits in the two crater palaeolakes of Trou au Natron at Pic Toussidé and Era Kohor at Emi Koussi. The two records cover the period from ~9500 to 4500 cal yr BP. Climate and palaeoenvironmental changes during this period were inferred from diatom assemblages, interpretation of variations in their oxygen isotope composition ($\delta^{18}O_{diatom}$), reconstruction of lake water conductivity from diatom-based transfer functions, and estimation of the lake water balance (Evaporation/Inflow ratio, E/I). Our findings provide evidence for two distinct lacustrine episodes. During the early to mid-Holocene transition, low $\delta^{18}O_{diatom}$ values, high percentages of planktonic diatoms, low lake water conductivity and a positive water balance ($E/I < 1$) suggest wet conditions, which were likely related to the optimum of the AHHP. From the mid-to late Holocene transition, an aridification trend is revealed by increasing $\delta^{18}O_{diatom}$ values, high percentages of benthic diatoms and a negative water budget ($E/I > 1$), occurring as early as 6500 cal yr BP and intensifying after 5300 cal yr BP. Moreover, our data show on average a decrease in precipitation amounts of ~35% between the peak and the end of the AHHP in the Tibesti region. This timing of the AHHP in the mountainous Tibesti is consistent with the aridification of the central Sahara recorded at lowland sites, which has mainly been related to the southward retreat of the Intertropical Convergence Zone (ITCZ) and the associated African monsoonal rainfall belt, following the gradually declining summer insolation that led to the termination of the AHHP. Our results prove the existence of Holocene lakes in the TVM craters that developed contemporaneously with the lakes of the Chadian basin and the Libyan Sahara. On a broader scale, our data share similar hydroclimatic patterns with studies from the eastern and northern Sahara.

1. Introduction

During the Holocene, African tropical and subtropical areas experienced extreme climatic variations (Gasse, 2000; Shanahan et al., 2015; Pausata et al., 2020) with a prolonged humid period referred to as the "African Humid Period" (AHP) (deMenocal et al., 2000), which in our paper is renamed the "African Holocene Humid Period" (AHHP). An extensive array of palaeoclimatic records (Shanahan et al., 2015; Holmes and Hoelzmann, 2017) and archaeological investigations (Cremaschi et al., 2014; Manning and Timpson, 2014) have shown that during this humid period, large parts of the present-day hyperarid Sahara and the semi-arid Sahel regions were much wetter and "greener" than today, and thus

* Corresponding author. Aix-Marseille Université, CNRS, IRD, INRAE, CEREGE, Aix en Provence, France.
E-mail address: yacoubabdallah@yahoo.fr (A.N. Yacoub).

https://doi.org/10.1016/j.quascirev.2023.108099

characterized by grasslands with tropical trees (Hély and Lézine, 2014), hosting numerous lakes (Hoelzmann et al., 2004; Drake et al., 2011) and incised by vast fluvial networks (Skonieczny et al., 2015). This early-to-mid Holocene period of greening of the Sahara, named the Green Sahara period (Claussen et al., 2017), was linked to the low precession in Earth's orbit associated with high boreal summer insolation that induced the northward extension of the Intertropical Convergence Zone (ITCZ) and the intensification of the associated African monsoonal rainfall belt (Kutzbach and Liu, 1997; deMenocal, 2015; Dallmeyer et al., 2020). These wetter conditions enabled widespread human occupation and the development of agriculture across North Africa (Kuper and Kröpelin, 2006; Manning and Timpson, 2014). After the mid-Holocene, the southward retreat of the monsoonal rainfall belt led to drier conditions that provoked the desiccation of most lakes (Gasse, 2000) and critical demographic shifts (Manning and Timpson, 2014), sealing the end of the AHHP. Throughout the African continent, the timing and magnitude of the termination of the AHHP were probably variable in space and time (Shanahan et al., 2015) and there is a long-standing and on-going debate about whether the end of the AHHP and the subsequent drying of the Sahara was abrupt or gradual (deMenocal et al., 2000; Holmes, 2008; Kröpelin et al., 2008; Bard, 2013; Collins et al., 2017; Ménot et al., 2020; Chase et al., 2022). However, while the main moisture source in this large part of the African continent is supposedly the summer monsoon belt (Kutzbach and Liu, 1997; Van der Meeren et al., 2022), some studies suggest additional sources such as Mediterranean air masses and/or the North and central Atlantic Ocean (Kutzbach et al., 2014; Cheddadi et al., 2021). In addition, rainfall linked to the seasonal tropical plumes associated with the Subtropical Jet Stream (Maley, 2000) may have contributed to the AHHP. Hence, several crucial aspects of the AHHP remain a matter of debate.

Due to their inner-continental position and their numerous lake deposits, the central Sahara and its forelands in Northern Chad are key regions for records of climatic changes. The lake deposits provide records of the wet conditions experienced during the AHHP that led to the establishment of the giant Lake Megachad (Ghienne et al., 2002; Schuster et al., 2005). However, despite several studies carried out in this part of Chad, (Amaral et al., 2013; Armitage et al., 2015; Bristow et al., 2018), no detailed palaeoclimatic data is available, largely owing to the lack of continuous and well-dated sedimentary records. Indeed, across this part of the Sahara most lake systems formed during the AHHP dried out at the end of the AHHP and lake deposits underwent eolian deflation, therefore eroding all or parts of the sedimentary records, leaving ubiquitous temporal hiatuses and making interpretation difficult (Gasse, 2000; Armitage et al., 2015). Well-preserved and continuous lake sedimentary records are critical for assessing climatic variations in the mountainous and lowland sites within the central Sahara in order to address: i) the temporal and spatial patterns of the AHHP; ii) potential palaeoclimate differences or similarities between mountainous and lowland regions; iii) local P-E quantifications.

Here, we provide palaeoclimatic data based on fossil diatoms extracted from sedimentary sequences collected in two high-elevation crater palaeolakes in the Tibesti volcanic massifs (TVC): the Trou au Natron, located at the foot of Pic Toussidé (~3315 m above sea level, asl) and the Era Kohor, located at the summit of Emi Koussi (~3415 m asl). Previous studies on well-stratified diatomites revealed that the Trou au Natron was occupied by a deep lake of at least 300 m depth (Maley, 2000; Soulié-Märsche et al., 2010). These studies assumed that the Tibesti palaeolakes existed during the late Pleistocene and that the establishment of deep lakes was a consequence of increased precipitation during this period. A recent study by Dinies et al. (2021) on Era Kohor crater palaeolake deposits showed that these palaeolakes are rather contemporaneous to the early to mid-Holocene period (thereby AHHP) and not of late Pleistocene age (Soulié-Märsche et al., 1995).

The main objective of this study is to provide the first $\delta^{18}O_{diatom}$ record from the central Sahara and investigate fossil diatom assemblages in order to better describe palaeoclimatic conditions in the Tibesti mountains during the AHHP. The $\delta^{18}O_{diatom}$ is commonly used as a climate proxy to quantify changes in past hydroclimate conditions (Leng and Barker, 2006; Quesada et al., 2015; Brown et al., 2021; Kostrova et al., 2021). The $\delta^{18}O_{diatom}$ is controlled by its forming water (i.e. the lake water) temperature and oxygen isotope composition (Moschen et al., 2005; Leng and Barker, 2006). Lake water conductivity is estimated using a diatom-based transfer function. A simple lake water mass balance model is used to assess the Evaporation/Inflow (E/I) ratio (Gibson et al., 2016; Cui et al., 2018). Thus the measured $\delta^{18}O_{diatom}$ values allow assumptions about the lake water isotope composition ($\delta^{18}O_{lake}$) and the E/I ratio, an informative lake water-balance metric (Broadman et al., 2022). Combining these variables and placing our records in a broader regional context, we address the climate history of the Tibesti Mountains during and at the end of the AHHP and discuss possible climatic synchronicity with other regions of the central Sahara and North Africa.

2. Regional and geological setting

The mountainous Tibesti massif, in the extreme northern part of Chad, extends from ~19° to 22°N of latitude and ~16° to 19°E of longitude (Fig. 1). Located halfway between the Mediterranean sea and Lake Chad, the massif also extends into southern Libya (Deniel et al., 2015; Elshaafi and Gudmundsson, 2021). In Chad, the Tibesti Volcanic Province (TVP) has a triangular surface area of about 100,000 km^2, and a third of its surface is covered by a thick mantle of volcanic formations. With elevations of more than 3000 m (asl), it is the highest massif of the Saharan Desert (Gourgaud and Vincent, 2004; Permenter and Oppenheimer, 2007). It has been poorly studied, mainly because of military conflicts and ongoing political instability which make fieldwork extremely hazardous and challenging (Deniel et al., 2015). Therefore, most of the literature is from early pioneering fieldwork (Wacrenier et al., 1958; Gèze et al., 1959; Vincent, 1963; Gavrilovic, 1969; Roland, 1974). More recently, fieldwork observations have been possible again in some parts of the Tibesti massif (Deniel et al., 2015; Ball et al., 2019; Dinies et al., 2021). Detailed available data on structural features and the geological history of the TVP are synthesized in Deniel et al. (2015 and references therein).

The western half of Tibesti forms a high plateau, punctuated by several craters, which are ignimbritic calderas (Maley, 2000). The Pic Toussidé appears to be one of the youngest volcanoes, with a height of ~3315 m and, in its south-eastern rim, the Trou au Natron caldera (~2300 m), an explosion-collapse caldera (Elshaafi and Gudmundsson, 2021). The crater is known as “Trou au Natron”, referring to the white deposits of sodium carbonate (salt-trona) that developed in the deepest part of the caldera due to the still active trona-springs (Maley, 2000).

The south-eastern part of the Tibesti is dominated by the highest summit in the Sahara: the Emi Koussi, a giant ignimbritic volcano, 3415 m high and 60–70 km in diameter (Deniel et al., 2015). At the summit, a depression of 11–15 km diameter consists of basalt and phonolite lava flows resulting from three successive Plio-Quaternary volcanic events and the subsequent collapse of three different calderas (Gourgaud and Vincent, 2004). The youngest and smallest is the Era Kohor caldera, 2 km in width with vertical walls of 300 m in height.

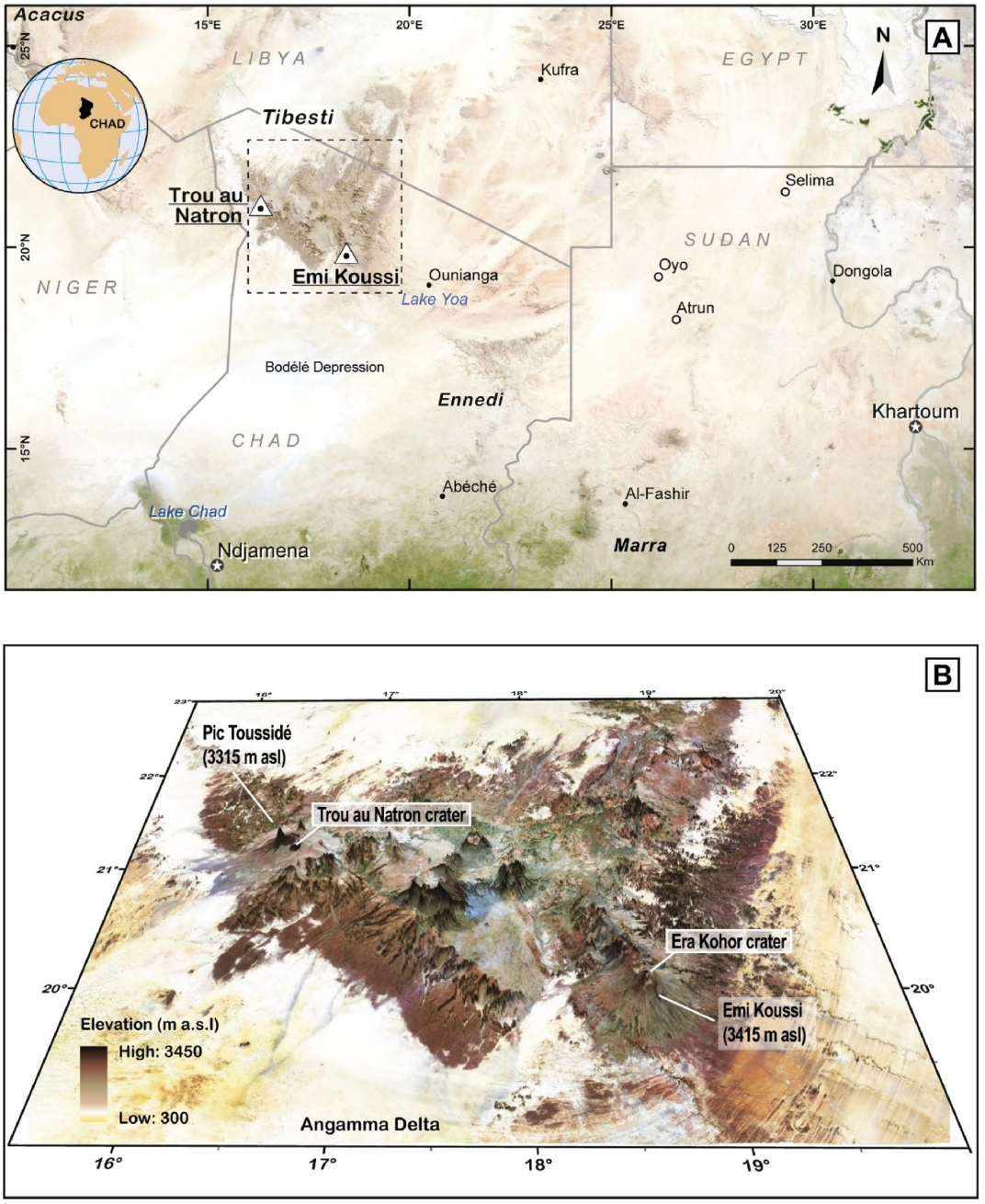

Fig. 1. Maps showing features and locations mentioned in the text. Panel A: The central Sahara and its southern transition to the Sahel, with the Tibesti and adjacent mountain massifs, Lake Yoa, and some other places with Holocene archives in Libya, Chad, and northern Sudan. Panel B: Oblique view of the Tibesti (dashed rectangle in Panel A, elevation x10) showing its general relief with the two highest peaks (Emi Koussi 3415 m asl, Pic Toussidé 3315 m asl) and the position of the investigated crater palaeolakes Era Kohor (~3300 m asl) and Trou au Natron (~2300 m asl). Data source: Modis, Landsat, SRTM (NASA).

The Tibesti mountains experience distinct patterns in terms of seasonal temperature gradients. The surrounding lower mountains and plains are characterized by mean annual temperatures ranging from 23 °C to 18 °C. However, in the mountain area a cold desert climate prevails with mean annual temperatures of ~13 °C, as recorded in the Trou au Natron by meteorological measurements (Gavrilovic, 1969). Present-day rainy events in the Tibesti mountains are erratic from year to year and the mean annual rainfall displays distinct patterns along the altitudinal gradient. For example, in the northern part, including the Trou au Natron, average annual precipitation is ~93 mm (Gavrilovic, 1969) with the rainiest and most humid events in August. Springtime rainfall of northerly origin also occurs in this region (Maley, 2000). In contrast, the southern slope, including the Emi Koussi, is characterized by a monsoonal

precipitation regime limited to July–August with an average of 45.9 mm annual rainfall (Maley, 2000).

3. Material and methods

3.1. Field campaign

Fieldwork was conducted in March 2015 and February 2016. The Trou au Natron (TN) crater's rim is about 8 to 6 km in diameter at an elevation between 2300 m and 2000 m asl (above sea level). Its floor lies at about 1540 m asl with no surficial outflow (Fig. 2A). Two well-preserved diatomaceous outcrops were sampled (Fig. 2a and b). The basal JK48 sequence is located 20 m above the floor of the crater and is about 300 cm thick. The W99 sequence is located 330 m above JK48 on the slope of the crater and is about 400 cm thick. The Era Kohor crater, located at the summit of Emi Koussi, has a diameter of about 2 km and a depth of ~300 m (Fig. 2A). The W566 sequence is located at about 120 m above the crater floor and is about 145 cm thick (Fig. 2c).

3.2. Lithology and chronology

The chronological framework of the Trou au Natron palaeolake was established using 6 sediment samples from the JK48 sequence and 6 sediment samples from the W99 sequence. They consist of *Tamarix* charcoals and concentrates of microscopic plant remains (pollen, charred plant particles, plant tissues) that were processed in the laboratory of the DAI Berlin (German Archaeological Institute). Sediment samples from selected depths without macroscopic charcoals were treated by combining different protocols to

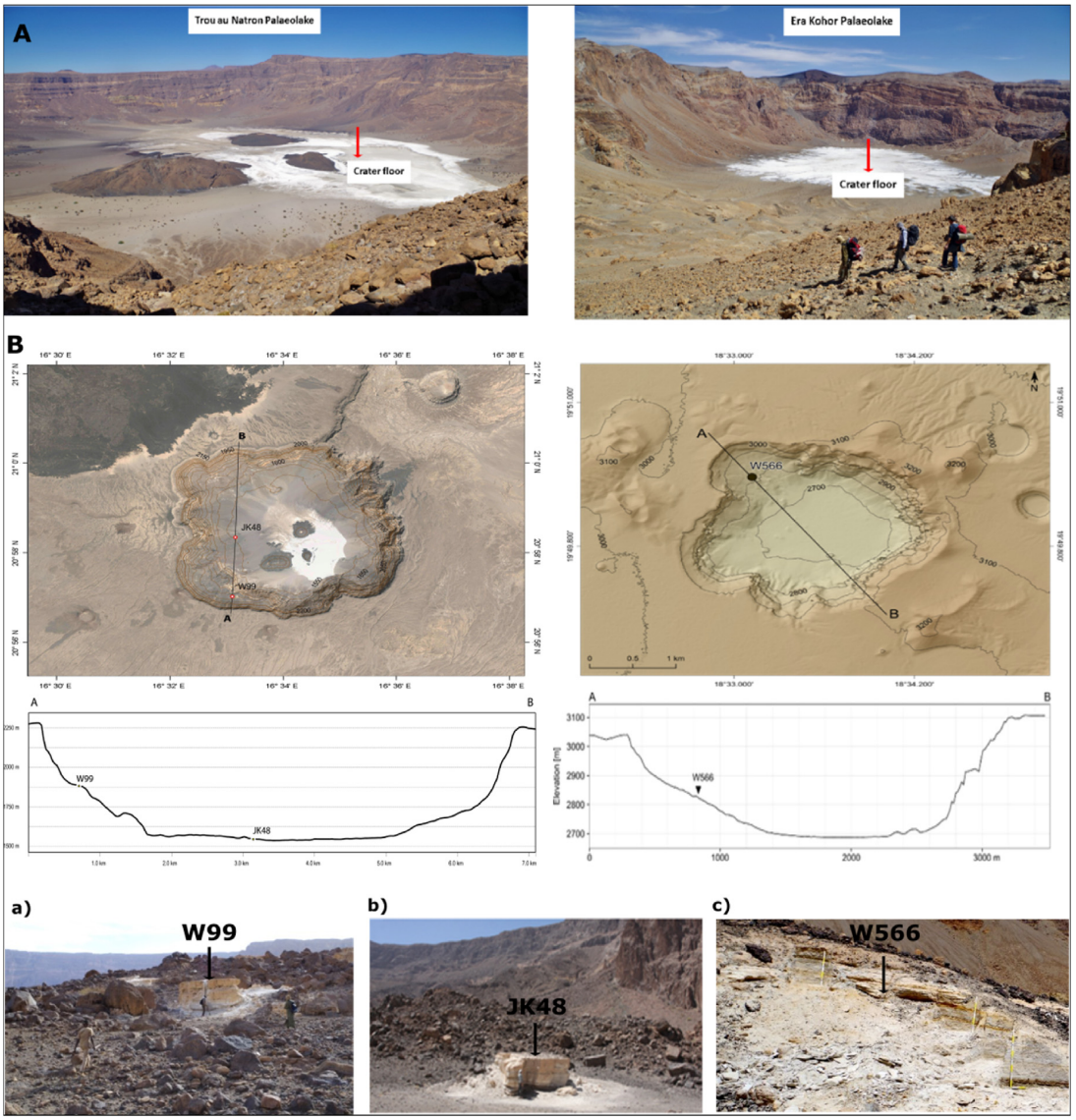

Fig. 2. Panel A: Field pictures of the two investigated Tibesti crater palaeolakes. Panel B: Google satellite images and topographic profiles of schematic sections of the investigated Tibesti palaeolakes and their respective craters with a) and b) (two left field pictures) showing the respective positions of the W99 and JK48 sedimentary sequences (indicated by vertical black arrows) within the Trou au Natron; c) (right field picture) showing the position of W566 sedimentary sequence (indicated by vertical black arrow) within the Era Kohor.

concentrate microscopic plant particles (Brown et al., 1992; Regnéll and Everitt, 1996; Vandergoes and Prior, 2003; Fletcher et al., 2017; Dinies et al., 2021). The preparation steps were: (1) Treatment with ~10% HCl (heated) to decalcify the sample, (2) Treatment with ~10% KOH (heated) to remove humic acids, (3) Dense-media separation with sodium-polytungstate (SPT; ~2,1 g/cm^3) to remove the minerogenic fraction (clay, silt and sand), (4) Microscopic analysis of the residues to decide on the next steps for the processing procedure, (5) Density separation (1.6–1.2 g/cm^3) with CsCl or repeated with 2.05–2.1 g/cm3 SPT, with microscopic control of the potential different phases. (6) Intermediary sieving with different mesh sizes (70 μm, 30 μm, 10 μm, 6 μm) was performed to determine concentration of microscopic plant particles if dense media separation failed. Based on the AMS-dates (Table 2), age-depth models were created for both sedimentary sequences using rbacon, a Bayesian approach with an implemented outlier analysis (Blaauw and Christen, 2011). Results are reported as calibrated radiocarbon years before present (cal yr BP), with 0 corresponding to 1950 CE (Common Era), using the latest calibration curve IntCal20 (Reimer et al., 2020). The ages and depths are given in Table 2. For the Era Kohor palaeolake (W566 sedimentary sequence), we used the sediment chronology and the age-depth model as developed, presented and discussed in the study by Dinies et al. (2021).

3.3. Fossil diatoms analysis

In total, 104 sediment samples, including 49 from the W566 sequence, 30 from the W99 sequence and 25 from the JK48 sequence, were analyzed to investigate their diatom assemblage composition. Samples were first prepared following the standard sediment treatment protocol (Battarbee et al., 2001). Organic and carbonate contents were removed with hot hydrogen peroxide (H_2O_2; 33%) and hot HCl (10%). For taxonomic identification and the counting of diatom species, a small quantity (~200 μl) of the cleaned sample was evaporated onto coverslips and then mounted on microscope glass slides using a high refractive index resin (Naphrax®). Diatom species were counted at ×1000 magnification using a Nikon Eclipse 80i microscope equipped with differential interference contrast optics. For each sample, a minimum of 500 diatom valves were counted along random transects. Taxonomic identification of diatoms followed Krammer and Lange-Bertalot (1986, 1988, 1991a, 1991b) and Gasse (1986) using the most recent revised nomenclature (Guiry and Guiry, 2022). Diatom taxa classification regarding preferred habitat drew on the ecological classification proposed by Gasse (1986) and the modern calibration recently conducted on the Chadian lakes (Rirongarti et al., 2022). Diatom habitats are categorized into planktonic and benthic species following Kostrova et al. (2021). Thus, the term benthic includes epipelic, epipsammic and epiphytic taxa. Facultative-planktonic taxa are included in the planktonic group. Diatoms, as highly sensitive indicator organisms, are rapidly affected by changes in lake depth, chemical conditions, nutrient and light availability (Wolin and Stone, 1999). As such, qualitative changes in diatom communities are expected to indicate changes in water levels and the hydrochemistry of water. Thus, the ratio of

Table 1
Climatic and hydrologic data used for the estimation of E/I ratio. TN = Trou au Natron and EK = Era Kohor. Values are expressed as annual averages.

Period	Variable	Value	Source
Modern data			
	Air temperature	(TN): 13 °C; (EK): 11 °C	Gavrilovic (1969)
	Relative humidity	20%	Deduced from POWER/NASA data
	Temperature lapse rate	−6.8 °C/km	Gavrilovic (1969)
	Precipitation $\delta^{18}O$	(TN): 6.2‰ VSMOW (EK): 8.1‰ VSMOW	Bowen and Wilkinson (2002)
Early to late Holocene (~10,000–4500 cal yr BP) data			
	Air temperature	(TN):14 °C (EK): 12 °C	LMDZ-iso model (Risi et al., 2010)
	Lake water T_L	(TN): 14 °C (EK): 12 °C	Assuming equilibrium between lake and atmosphere (no offset between the lake and air temperature)
	Lake water $\delta^{18}O$	‰ VSMOW	Estimated from $\delta^{18}O_{diatom}$ (Crespin et al., 2010, corrected in Alexandre et al., 2012)
	Relative humidity	20%	Deduced from POWER/NASA data and LMDZ-iso model (Risi et al., 2010)
	Precipitation $\delta^{18}O$	(TN): 6.2‰ VSMOW; (EK): 8.1‰ VSMOW	Estimated from Bowen and Wilkinson (2002) assuming no changes in $\delta^{18}Op$ since Holocene according to the LMDZ-iso model (Risi et al., 2010) and Gasse (2002)

Table 2
Depths and ages of the charred particles for the JK48 and W99 sequences from Trou au Natron palaeolake.

Sequence ID	Depth below the surface (cm, midpoint)	Lab ID	Material dated	^{14}C yr BP	cal yr BP (2σ)
W99	63.5	Beta-423374	*Tamarix* charcoal	4520 ± 30	5050–5309
W99	106.5	Beta-423375	*Tamarix* charcoal	5090 ± 30	5746–5914
W99	208	Poz-122316	Concentrate of charred plant particles	6210 ± 40	6990–7251
W99	275.5	Beta-453615	*Tamarix* charcoal	6330 ± 30	7165–7320
W99	288.5	Poz-125904	Concentrate of charred plant particles	6500 ± 50	7310–7559
W99	295.5	Poz-122315	Concentrate of charred plant particles	6080 ± 80	6746–7162
JK48	40.5	Beta-453611	Not charred plant fragment	5430 ± 30	6191–6295
JK48	128.5	Poz-126143	Concentrate of charred plant particles	6860 ± 130	7489–7957
JK48	151.5	Poz-122363	Concentrate of charred plant particles	7540 ± 50	8200–8419
JK48	196.5	Beta-470620	Concentrate of charred plant particles	7320 ± 60	8009–8318
JK48	221.5	Poz-122364	Concentrate of charred plant particles	8640 ± 40	9535–9690
JK48	221.5	Poz-122317	Concentrate of charred plant particles	8570 ± 110	9296–9905

planktonic to benthic (P/B), which is known to reveal changes in lake level fluctuations (Brown et al., 2021), was calculated for each sample.

3.4. Inferred conductivity from diatom-based transfer function

In the Tibesti area, no calibration function is available to infer water salinity from fossil diatom assemblages. A diatom-inferred conductivity transfer function was recently developed for the lakes of the Ounianga system (Rirongarti et al., 2022). However, the Tibesti fossil assemblages contain a great number of diatom taxa that are not found in the Ounianga modern training dataset, thus preventing a robust application. Therefore, we employed a diatom-based conductivity transfer function from a modern semi-hemispheric African dataset (Gasse et al., 1995), which has been widely used (Kröpelin et al., 2008; Roubeix and Chalié, 2019) and which displays a sufficient diatom taxa overlap with our fossil data. The training dataset used for the reconstructed palaeosalinity (approached via the conductivity and expressed in $\log_{10}$ µS cm^{-1}) consists of 282 modern samples from about 150 African sites, in which 400 species were selected as being statistically valuable (Gasse et al., 1995). Transfer function development and conductivity inferences were carried out using the computer program C2 v.1.7.2 (Juggins, 2007). We used the Weighted Averaging Method (WAM) from ter Braak and Looman (1986). Taxonomic correspondences and synonymies of species between fossil and modern data were carefully established. As such, 95% of the species present in the Tibesti sequences were included in the transfer function procedure.

3.5. Diatom oxygen isotope composition analysis ($\delta^{18}O_{diatom}$)

For diatom oxygen isotope ($\delta^{18}O_{diatom}$) measurements, a total of 69 sediment samples from the three sequences (30 in W566, 23 in W99 and 16 samples in JK48) were processed using chemical and physical preparation steps as detailed in Crespin et al. (2008, 2010). After the cleaning process, the purity of diatom samples and signs of dissolution were checked using optical and scanning electron microscopies (SEM) (Fig. 3).

Additionally, elemental semi-quantitative micro-X-ray fluorescence (micro-XRF) analyses were performed using a HORIBA XGT-5000177 microscope. To ensure that samples were devoid of any terrigenous matter, samples were checked through X-ray diffraction (XRD) using X PANalytical (X'Pert Pro). For isotope analysis, 1.6 mg of purified diatoms were dehydrated and dehydroxylated under a flow of N_2 (Chapligin et al., 2010) and oxygen extraction was performed using the IR Laser-Heating Fluorination Technique (Alexandre et al., 2006; Crespin et al., 2008). The extracted oxygen gas was sent directly to a dual inlet mass spectrometer (Thermo-Quest Finnigan Delta Plus). The measured $\delta^{18}O_{diatom}$ values were corrected on a daily basis using a laboratory quartz standard ($\delta^{18}O_{boulangé\_50-100\ µm}$) calibrated on NBS28. The long term $\delta^{18}O$ average obtained for NBS28 is 9.678‰ ± 0.187 (n = 12). The data are expressed in the standard δ-notation relative to VSMOW.

3.6. Hydrologic and isotope mass balance modeling

3.6.1. Lake water balance (E/I) modeling

In order to further quantify the past hydrological fluctuations of the palaeolakes, a simple lake water balance model for estimating the E/I ratio was applied (Gibson et al., 2016; Cui et al., 2018).

The hydrologic (Eq. (1)) and isotope (Eq. (2)) mass balance model of a lake in a steady state for a given time can be expressed as follows:

$$P + Qi = E + Qo \tag{1}$$

$$(P + Qi)\,\delta I = E\,\delta E + Qo\delta L \tag{2}$$

where P and Qi are water inputs by direct precipitation and from the watershed respectively, E is the total evaporation, Qo is the surface outflow and underground leakage, δL is the $\delta^{18}O$ of the lake water, δI is the $\delta^{18}O$ of water inputs and δE is the $\delta^{18}O$ of the evaporation flux.

Based on the isotope and water mass balance equations, we determined the E/I lake water balance using I = P + Qi, following Gibson and Edwards (2002):

$$\frac{E}{I} = \frac{(\delta L - \delta I)}{(\delta L - \delta E)} \tag{3}$$

3.6.2. Lake water oxygen isotopic composition ($\delta^{18}O_{lake}$)

To calculate the past oxygen isotope composition of lake water ($\delta^{18}O_{lake}$) from measured $\delta^{18}O_{diatom}$ both lake water temperature (T_L) and the isotopic fractionation between water and diatoms are required. Assuming that diatom frustules precipitate in equilibrium with their forming water, a thermo-dependent relationship links

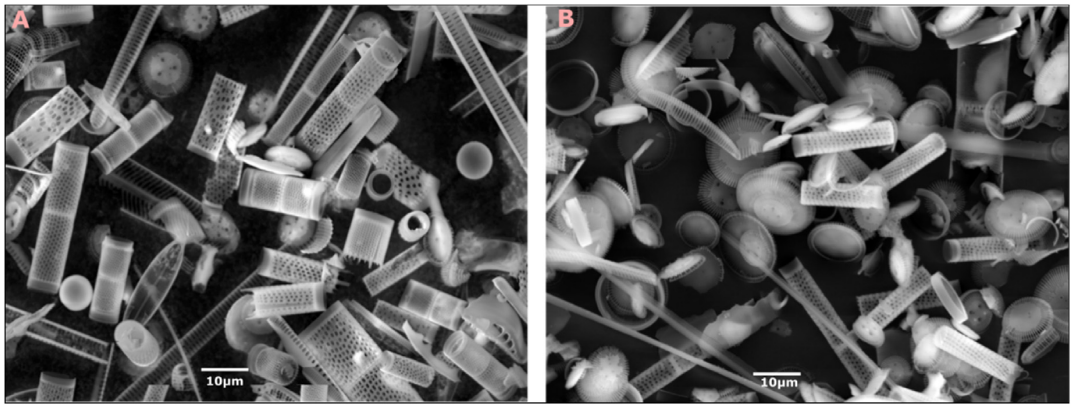

Fig. 3. SEM images of purified diatom biogenic silica (main displayed species *Aulacoseira granulata* and *Pantocsekiella ocellata*) from samples (A) W99-234-235 (~7020 cal yr BP) and (B) JK48-36-37 (~8960 cal yr BP). No mineral grains or signs of dissolution are visible, indicative of the high degree of purity of the samples.

$\delta^{18}O_{diatom}$ and $\delta^{18}O_{lake}$ (Moschen et al., 2005; Crespin et al., 2010; Dodd and Sharp, 2010):

$$[\delta^{18}O_{diatom} - \delta^{18}O_{lake}]\ (‰\ vs\ VSMOW) = a.T_L(°C) + b, \quad (4)$$

where $\delta^{18}O$ values are in ‰ vs VSMOW and T_L is in °C.

In the present study, this corrected equation with a fractionation factor of −0.28‰/°C obtained from freshwater diatoms and previously used for $\delta^{18}O_{lake}$ reconstructions (Quesada et al., 2015; Broadman et al., 2022) is considered to capture the relationship between $\delta^{18}O_{diatom}$, T_L and $\delta^{18}O_{lake}$ at high altitude sites such as the Tibesti mountains.

T_L is assumed to be constant during the investigated period and equivalent to air temperature on the annual scale (Adallal et al., 2019). As we focus on the evolution of the proxies rather than on their absolute values, this assumption appears reasonable. The annual average air temperature recorded from 1965 to 1968 CE at the Trou au Natron station (Gavrilovic, 1969) was used for estimating the modern T_L. For the Era Kohor, meteorological data from the Bardaï station (located within the Tibesti low mountains) are available. Given the altitudinal difference between Bardaï (altitude: ~1000 m asl) and the Emi Koussi (altitude: >3000 m asl), and a temperature lapse rate of −6.8 °C/km (Gavrilovic, 1969), the modern annual average air temperature at Era Kohor can be deduced. According to the LMDZ-iso model (Risi et al., 2010), the difference in air temperature between the mid-Holocene and the modern day is very low in most regions. For the Tibesti mountains, the model suggests a decrease in temperature of ~1 °C−1.5 °C from the early to mid-Holocene. Thus, based on the above assumptions, we estimated a constant average annual air temperature and T_L for the Trou au Natron (14 °C) and the Era Kohor (12 °C) palaeolakes for the investigated period.

3.6.3. Precipitation isotopic composition ($\delta^{18}Op$)

Since no precipitation isotope data appropriate to the study focus are available, we calculated annual $\delta^{18}Op$ values for modern rains using the equation from Bowen and Wilkinson (2002), established from the International Atomic Energy Agency (IAEA)-World Meteorological Organization (WMO) Global Network for Isotopes in Precipitation (GNIP) database (IAEA/WMO, 1998) and describing the isotopic composition of precipitation ($\delta^{18}Op$) for the continents as controlled by latitude (LAT) and altitude (ALT). For stations located >200 m asl, the equation is expressed as follows:

$$\delta^{18}Op = -0.0051(|LAT|)^2 + 0.1805(|LAT|) - 0.002(ALT) - 5.247 \quad (5)$$

Turning to past periods, we used the LMDZ-iso model (Risi et al., 2010) to estimate the $\delta^{18}Op$ from the calculated modern $\delta^{18}Op$ data. According to this model and other regional isotopic data (Gasse, 2002), the isotopic composition of Holocene rainfall did not differ significantly from that of the present day in areas such as the Tibesti region. Thus, we assume that the modern-day $\delta^{18}Op$ estimates resemble Holocene $\delta^{18}Op$ values.

3.6.4. Evaporative flux isotopic composition (δE)

Estimating δ_E in past hydrological lake water balance modeling is a challenging task. This flux is depleted in heavy isotopes relative to the lake water, mainly depends on kinetic fractionation, and is the main parameter in the isotopic balance of a lake (Vallet-Coulomb et al., 2008). Usually, it is deduced from the Craig and Gordon (1965) model as follows:

$$\delta_E = \frac{\delta_L - h\delta_A - \varepsilon}{1-h} \quad (6)$$

where h is the relative humidity, δ_L is the isotopic composition of lake water, δ_A is the isotopic composition of the atmospheric vapor, and (ε) is the total isotopic enrichment factor accounting for both kinetic (ε_k) and equilibrium (ε^*) enrichment ($\varepsilon = \varepsilon^* + \varepsilon_k$). The kinetic fractionation coefficient (ε_k) can be approximatively estimated as follows:

$$\varepsilon_k = \theta.\ C_k\ (1 - h) \quad (7)$$

With (ε_k) expressed as a function of the relative humidity (h), the parameter C_k (which is a "kinetic" constant dependent on the model) is determined experimentally as $C_k = 14.2‰$ for $\delta^{18}O$ in the case of evaporation from a free water surface (Gonfiantini, 1986). θ is an empirical term, representing the turbulent component. The normalized relative humidity (h) is estimated using data obtained from the Prediction of Worldwide Energy Resource (POWER/NASA) (https://power.larc.nasa.gov/). The isotope composition of atmospheric moisture (δ_A) is deduced from the LMDZ-iso model (Risi et al., 2010). Detailed information about the data used to resolve these equations is provided in Table 1.

4. Results

4.1. Lithology and chronology

The basal deposits of the JK48 and W99 sequences from the Trou au Natron consist of sand and gravel. In JK48, they are overlayed by diatomaceous siltstone, becoming increasingly calcareous, with the highest carbonate contents 37−62 cm below the top of the section. In the W99 sequence, 330 m above, limy diatomaceous siltstone dominates the sequence (Fig. 4). Similarly, the W566 sequence from the Era Kohor is characterized by sand and gravels in its basal part followed by varying proportions of silty diatomite.

All available ^{14}C-dates, the concentrates of plant micro-remains and the *Tamarix* charcoals were included in the age-depth model (Table 2), resulting in a roughly linear age-depth model (Fig. 4). Two ^{14}C-dates secure the basal age of the JK48 deposit. The only dating mismatch with the modeled age-depth relation is at a depth of about 200 cm below the surface. Since charred plant particles were also dated from this depth, the offset is difficult to explain. However, the consistent two basal datings on two fractions from the same depth (unspecified charred plant particles and the outermost layer with cuticula of plants), as well as the match of the remaining dating, indicate the reliability of the roughly linear model. The dating result near the basis of W99 overlaps the dating a few centimeters above and thus fits the age-depth model. No datable material was available for the basis of W99, composed of sand and gravel. Ages for these ~20 cm were extrapolated, despite the difficulty of extrapolation especially when there is a sediment change. However, because these basal sand and gravel sediments are devoid of diatoms, no samples from this extrapolated section were analyzed in this study.

For the JK48 sequence, the basal age is extrapolated to the early Holocene (~10,000 cal yr BP) and covers the period ranging from ~10,000−5500 cal yr BP. For the W99 sequence, the oldest ^{14}C age is 6500 ± 50 cal yr BP. The model produces an extrapolated age for the basal sample of 7500 ± 30 cal yr BP. Thus, the W99 sequence covers the period ~7500-4500 cal yr BP. For Era Kohor, the W566 sequence covers approximately the period 9500−5500 cal yr BP, as detailed in Dinies et al. (2021).

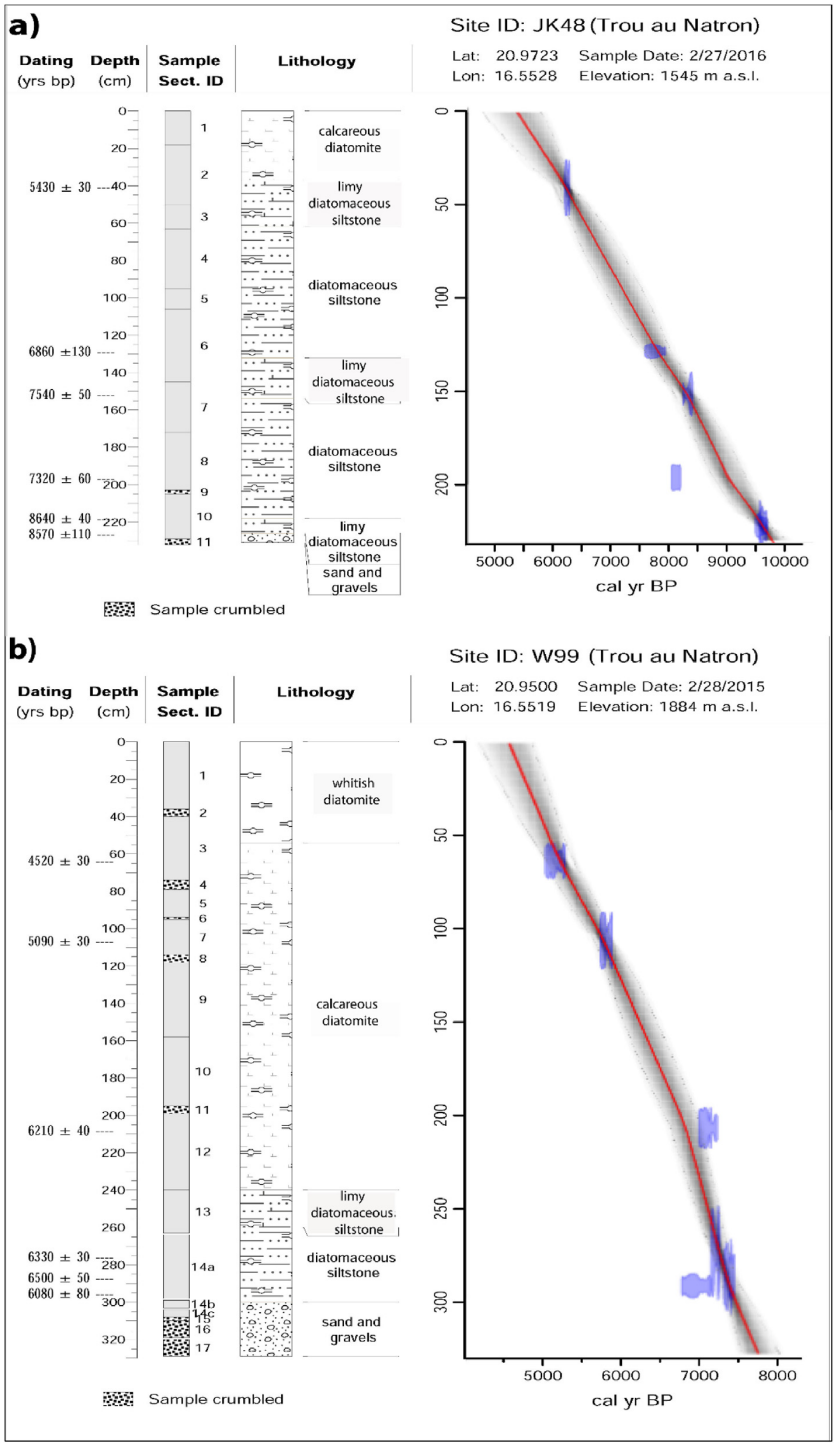

Fig. 4. Stratigraphy of Trou au Natron palaeolake sequence JK48 (a) and W99 (b) with lithology, sample section (crumbled or not), depth (cm), calibrated ^{14}C ages, and the age-depth models, created using rbacon (v.2.4.3; Blaauw and Christen, 2011).

4.2. The Trou au Natron palaeolake

4.2.1. Composition of the fossil diatom assemblages

In the JK48 sequence, a total of 27 diatom taxa belonging to 16 genera were identified. A stratigraphic diagram of their relative abundance exhibited three diatom assemblage zones (DZI to DZIII in Fig. 5). Between ~9500 and 8000 cal yr BP (JK48-DZI), freshwater planktonic species such as *Aulacoseira granulata* and *Pantocsekiella*

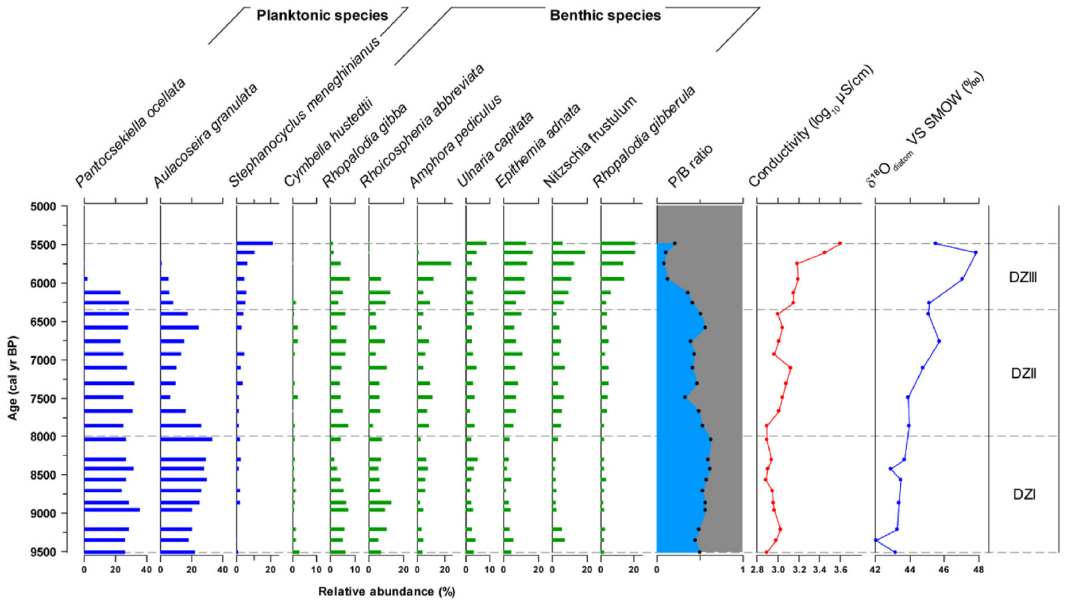

Fig. 5. Stratigraphic diagram of diatom abundances in the JK48 sequence from Trou au Natron: relative abundances of dominant diatom species grouped by habitat preference, planktonic to benthic ratio (P/B), lake diatom-inferred conductivity and the oxygen isotopic composition of fossil diatoms ($\delta^{18}O_{diatom}$).

ocellata dominated (~45–62%). Benthic species (~38–55%) were mainly represented by *Rhopalodia gibba, Rhoicosphenia abbreviata* and *Amphora pediculus* to a lesser extent. Other benthic taxa such as *Epithemia adnata, R. gibberula, Nitzschia frustulum, Cymbella hustedtii* and *Ulnaria capitata* occurred in low abundances. In JK-48 DZII (8000-6300 cal yr BP) planktonic *P. ocellata* was still present in similar proportions to those in DZI, while *A. granulata* declined and *Stephanocyclus meneghinianus* started to develop. Benthic taxa were the same as in DZ1 but *E. adnata*, *N. frustulum* and *R. gibberula* were more abundant. With other benthic *Cocconeis placentula, Amphora ovalis, Diploneis subovalis* and *Ulnaria capitata*, they represented up to 60% of the flora. The JK48-DZIII zone (6300-5500 cal yr BP) was characterized by the decline of planktonic forms at the expense of benthic taxa, starting between ~6300 and 6000 cal yr BP. Benthic taxa dominated this zone (~93%). While *E. adnata*, *N. frustulum*, *R. gibberula* and *Amphora pediculus* developed, *R. gibba, R. abbreviata and C. hustedtii* receded. After ~5800 cal yr BP, planktonic *P. ocellata* and *A. granulata* gradually disappeared while the facultative planktonic *S. meneghinianus* (up to 22%) associated with the tychoplanktonic *Ulnaria capitata* (3–9%) developed.

Within the W99 sequence, 30 species were identified and distributed among 16 genera. A stratigraphic diagram of their relative abundance revealed three diatom assemblage zones (Fig. 6). The diatom flora of the W99 site was very similar to those of site JK48, although it represented a more recent time interval. Between ~7500 and 6300 cal yr BP, the W99-DZI zone was characterized by fluctuating co-dominant planktonic (~40–55%) and benthic species (~45–60%) as shown in the P/B ratio (Fig. 6). Planktonic species were again represented by *A. granulata* and *P. ocellata*. As in JK48, benthic forms were represented by *E. adnata, A. pediculus, R. abbreviata, R. gibba, C. placentula, D. subovalis, C. hustedtii,* and *U. capitata*. However, just before ~6500 cal yr BP, benthic species progressively increased at the expense of planktonic species. In the W99-DZII zone (~6300 and 5200 cal yr BP), the trend of increased benthic species initiated in the W99-DZI zone continued while planktonic *A. granulata* gradually declined and *P. ocellata* persisted (20–25%). The benthic assemblage, composed of *R. abbreviata, E. adnata, A. pediculus, A. ovalis* and *C. placentula,* reached up to >70% at the end of the zone while planktonic species markedly declined. In the W99-DZIII zone (~5200–4500 cal yr BP), benthic species kept developing to reach ~100% of the flora just after ~5000 cal yr BP. The benthic assemblage was similar to that of the W99-DZII zone with the exception of the decline of *D. subovalis*. Planktonic *A. granulata* disappeared while *P. ocellata* was poorly represented.

4.2.2. Diatom-inferred conductivity

In the following section, we report the outcomes in $\log_{10}$(conductivity) units, accompanied by the corresponding raw conductivity values enclosed in brackets. It is important to note that these reconstructed log-transformed values should not be considered equivalent to the values that could be derived from a direct diatom-conductivity transfer function.

Diatom-inferred conductivities from the JK48 sequence (Fig. 5) exhibited low values at the base of the sequence and gradually increased upwards. From ~9500 to 8000 cal yr BP, low conductivity values averaging 2.9 $\log_{10}$ µS/cm (~790 µS/cm) correspond to a lake dominated by planktonic species. After 8000 cal yr BP, conductivities showed an increasing trend until ~6300 cal yr BP with average values of 3.01 $\log_{10}$ µS/cm (~1020 µS/cm). After ~6300 cal yr BP the conductivity markedly increased to reach a maximum of 3.60 $\log_{10}$ µS/cm (~3980 µS/cm) at ~5470 cal yr BP.

In the W99 record, diatom-inferred conductivities (Fig. 6) ranged from 2.77 $\log_{10}$ µS/cm (~590 µS/cm) to 3.0 $\log_{10}$ µS/cm (~1000 µS/cm) and were of a slightly lower order than those of the JK48 sequence. However, in the W99 between ~7500 and 6300 cal yr BP, conductivities values fluctuated more than in the JK48 sequence despite averaging 2.85 $\log_{10}$ µS/cm (~710 µS/cm). After ~6300 cal yr BP, the conductivity increased to reach a maximum of 3.0 $\log_{10}$ µS/cm (~1000 µS/cm) at ~5000 cal yr BP. Thereafter, conductivity remained relatively stable with only minor

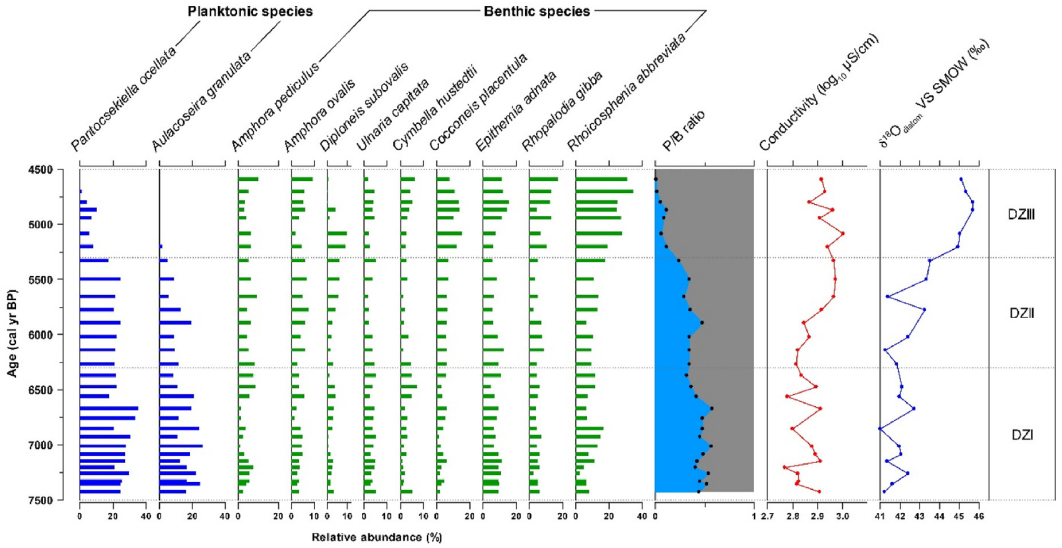

Fig. 6. Stratigraphic diagram of diatom abundances in the W99 sequence from Trou au Natron: relative abundances of the dominant diatom species grouped by habitat preference; planktonic to benthic ratio (P/B); the diatom-inferred lake conductivity and the oxygen isotopic composition of fossil diatoms ($\delta^{18}O_{diatom}$).

fluctuations at the top of the sequence at ~4500 cal yr BP.

4.2.3. Oxygen isotopic composition of fossil diatoms ($\delta^{18}O_{diatom}$)

In the JK48 record, the $\delta^{18}O_{diatom}$ values were between ~42‰ and ~48‰ (Fig. 5), showing an increasing trend from the base of the sequence to the top. In the basal JK48-DZI zone, the $\delta^{18}O_{diatom}$ values were the lowest (42.03 and 42.91‰) at ~9300 and ~8400 cal yr BP respectively. In the DZII zone, $\delta^{18}O_{diatom}$ increased from 44.76‰ at ~7100 cal yr BP to 45.08‰ at ~6400 cal yr BP. In the DZIII zone, the $\delta^{18}O_{diatom}$ values increased sharply by ~2‰ to reach the highest values (47.05‰ and 47.86‰) at ~6000 and ~5600 cal yr BP respectively.

The $\delta^{18}O_{diatom}$ values from the W99 record were between ~41‰ and ~46‰ (Fig. 6) and relatively lower than those of JK48. Overall, an increasing trend in $\delta^{18}O_{diatom}$ values along the sequence was observed in both records. From ~7500 to 6300 cal yr BP, the $\delta^{18}O_{diatom}$ values were low and centered around 41.01‰. Between 6300 and 4800 cal yr BP, $\delta^{18}O_{diatom}$ values displayed an increasing trend up to ~43.3‰ although two drops (41.27‰ and 41.42‰) were observed at ~6150 cal yr BP and ~5650 cal yr BP respectively. After ~5300 cal yr BP, the $\delta^{18}O_{diatom}$ values increased from 45.01‰ at ~5000 cal yr BP to reach a maximum (45.71‰) at ~4800 cal yr BP.

4.3. The Emi Koussi palaeolake

4.3.1. Composition of the fossil diatom assemblages

The W566 sequence was characterized by more diversified diatom flora than that of the Trou du Natron: 65 species from 19 genera, although the dominant species remained the same. However, the striking feature of this sequence was the almost equal proportions of planktonic and benthic forms. Based on a stratigraphic diagram of their relative abundances, three zones could be identified (Fig. 7).

The base of W566-DZI (~9400 cal yr BP) was dominated (up to 75%) by freshwater planktonic *Aulacoseira* spp. (*A. granulata, A. granulata* var. *angustissima, A. ambigua*) and *P. ocellata*. From ~9300 cal yr BP to ~9200, an abrupt decrease in planktonic forms occurred concomitantly with a rise in benthic forms (see P/B ratio). Thereafter, the diatom assemblage was co-dominated by benthic and planktonic species. Freshwater benthic taxa were represented by *E. adanata, R. gibba, Mastogloia elliptica, U. capitata, C. placentula* and *D. subovalis*. In the W566-DZII zone (~8000-6400 cal yr BP), the diatom assemblage was dominated by the same benthic species while planktonic *P. ocellata* developed again. In the DZIII zone (~6400-5500 cal yr BP), the relative abundance of planktonic diatom slightly decreased.

4.3.2. Inferred conductivity from the diatom-based transfer function

The diatom-inferred conductivities of the Emi Koussi sequence were of the same order as those of the Trou du Natron, between 2.7 and 3.14 $\log_{10}$ µS/cm (~500 and 1380 µS/cm) (Fig. 7). Although the conductivity fluctuated significantly throughout the W566 sequence (Fig. 7), most of the values lay between 2.8 and 3.0 $\log_{10}$ µS/cm (~630 and ~1000 µS/cm). Rapid drops were recorded at ~9150, ~8500 and 7100 cal yr BP. Conversely, an episode of increased conductivities occurred between ~9000 and 8500 cal yr BP and ~8000-6400 cal yr BP. After ~7000 cal yr BP, conductivity values rose rapidly to reach 3.14 $\log_{10}$ µS/cm (~1380 µS/cm) at ~6500 cal yr BP and then remained relatively high until ~ 5500 cal yr BP.

4.3.3. The oxygen isotopic composition of fossil diatoms ($\delta^{18}O_{diatom}$)

The $\delta^{18}O_{diatom}$ values of the W566 sequence were lower than those of the Trou du Natron and ranged from ~32‰ to ~41‰ with an average value of ~36‰ (Fig. 7). Similarly to the conductivity values, $\delta^{18}O_{diatom}$ values fluctuated throughout the sequence. However, a general trend in increasing value was noticeable. At ~9340 cal yr BP, relatively low $\delta^{18}O_{diatom}$ values of ~32.28‰ were followed by an abrupt increase to 35.17‰. The interval ~8000–6500 cal yr BP was characterized by regular fluctuations in $\delta^{18}O_{diatom}$ values. Between ~6400 and ~5800 cal yr BP, higher $\delta^{18}O_{diatom}$ values averaging 37.41‰ were recorded. Then, at ~5500 cal yr BP, the maximum value of 40.61‰ was reached, although this should be considered with caution since it was measured from a reworked sample of ~15 cm thickness.

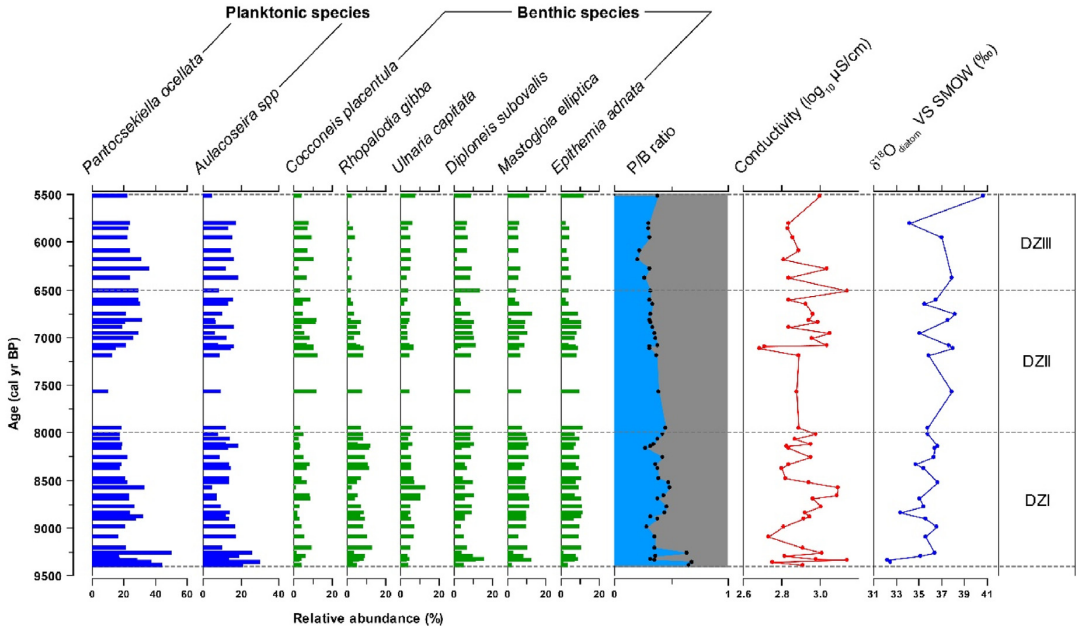

Fig. 7. W566 sequence from Emi Koussi: Stratigraphic diagram of dominant diatom species grouped by habitat preference; planktonic to benthic ratio (P/B); diatom-inferred lake conductivity; oxygen isotopic composition of fossil diatoms ($\delta^{18}O_{diatom}$).

5. Discussion

5.1. Proxy evidence and lake water balance

To assess the lake water balance of the Tibesti crater palaeolakes we employed a quantitative model that displays an E/I ratio ranging from <1 (i.e., higher precipitation) to >1 (i.e., drop in the lake level due to increased evaporation) and that fits well with diatom assemblages (P/B ratio), oxygen isotopic composition ($\delta^{18}O_{diatom}$) and inferred lake conductivity (Fig. 8).

From ~9500 to 7500 cal yr BP, the records show concomitantly low $\delta^{18}O_{diatom}$ values, a positive lake water balance (E/I < 1; Fig. 8i and j) and low $\delta^{18}O_{lake}$ values (Fig. 8e and f), suggesting high moisture conditions associated with monsoon air masses and/or tropical depressions that produce ^{18}O-depleted values (Fontes et al., 1993). Moreover, fossil diatom assemblages provide additional evidence of a wet episode. The dominance of two planktonic freshwater species, *A. granulata* and *P. ocellata* (high P/B ratio) suggests a deep and permanent lake (Fig. 8a and b). At this time, low water conductivities supported freshwater lake conditions (Fig. 8c and d), in agreement with similar diatom-inferred chemical variables reported from the nearby northern Niger palaeolakes (Gasse, 2002). This lake highstand is consistent with the wet conditions derived from palynological data (Dinies et al., 2021), which show a high humidity index from the Era Kohor palaeolake. The timing of a moist stage in the Tibesti mountains seems to coincide with the optimum of the AHHP as seen elsewhere in the central Sahara (Gasse, 2000; Cremaschi et al., 2014; Armitage et al., 2015; Bristow et al., 2018). Moreover, the positive water balance recorded in the Trou au Natron and the Era Kohor palaeolakes is also consistent with the evidence of enhanced precipitation in the Sahara between 10,000 and 8000 cal yr BP (Tierney et al., 2017). At that time, the Tibesti mountains might have acted as topographic barriers to the northern expansion of monsoonal air masses inducing high summer precipitation. Because of this geological configuration, the Tibesti may have also facilitated the penetration of Mediterranean winter humid air masses further south than is the case today, between 18°N and 24°N, as shown by Cheddadi et al. (2021), leading to two rainy seasons over the central Sahara during the Holocene, as already suggested by Fontes et al. (1993).

From ~7500 to 6000 cal yr BP, the lake at Trou au Natron experienced a slight increase in evaporation (E/I ratio), leading to somewhat high $\delta^{18}O_{diatom}$ and lake water conductivity. These characteristics are the first signs of aridification that were likely linked to reduced precipitation, as revealed by the increasingly negative water balance (Fig. 8c and d; g and h). After 6000 cal yr BP, the lake experienced drops in water level that favored the development of benthic forms which then became as abundant as planktonic species. The lowering of the lake level is supported by the slightly increased $\delta^{18}O_{diatom}$ values accompanied by an increasingly negative water balance, as seen in the Trou au Natron palaeolake. Meanwhile, the Era Kohor palaeolake experienced positive and negative fluctuations in the water balance, associated with a slightly increasing trend in $\delta^{18}O_{diatom}$, together with a relative increase in water conductivity. The diatom assemblage was dominated by benthic forms while planktonic taxa gradually receded, reflecting a low-stand lake. Although expressed with different intensities and magnitudes in the Trou au Natron and the Era Kohor palaeolake records, these variables can be interpreted as signs of aridification. The water balance (E/I ratio) and the inferred freshwater character of the Tibesti lakes at the time are indeed coherent with those observed for the central Sahara and the Sahel lowlands (Gasse, 2002).

From ~6000 to ~5500 cal yr BP, the Trou au Natron and the Era Kohor palaeolake records show higher $\delta^{18}O_{diatom}$ values and a shift towards a gradually negative water budget (E/I > 1), supporting the progression of aridification. This shift towards drier conditions is also evidenced by the decline in planktonic diatoms, which was likely due to a shortage of freshwater supply resulting from reduced precipitation in the surroundings. Diatoms that thrived at the time in the Trou au Natron were mainly benthic forms, which included many epiphytic taxa such as *A. pediculus, E. adnata, N. frustulum, R.*

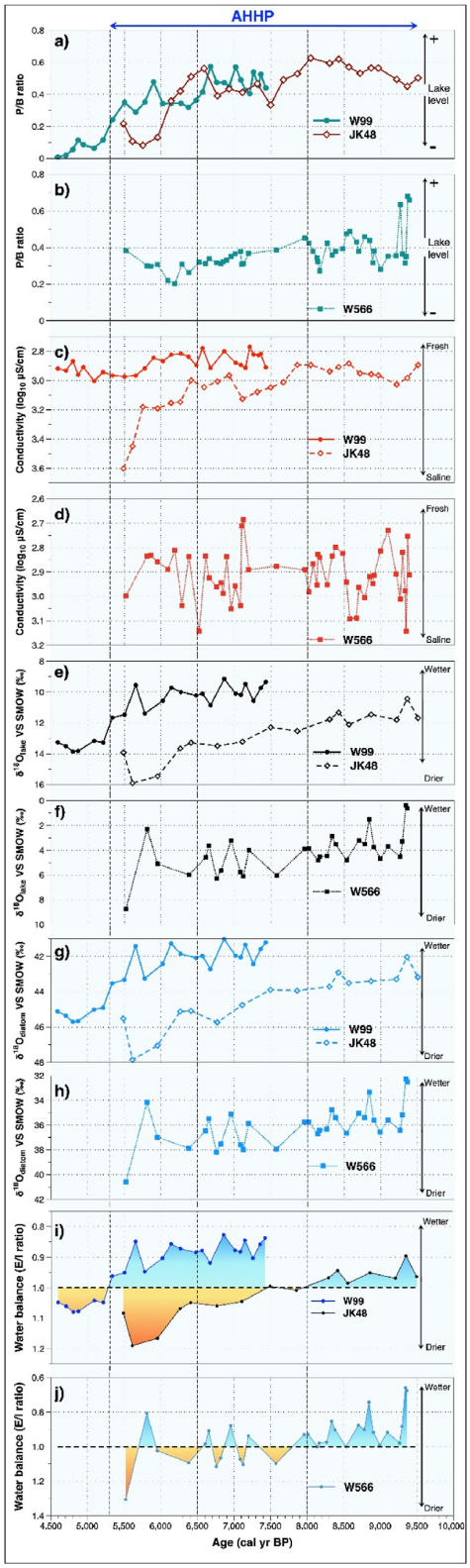

gibba, R. abbreviata and *C. placentula*. Similarly, in the Era Kohor palaeolake, benthic forms dominated with a fair proportion of planktonic diatoms, reflecting the gradual lowering of permanent water. Specifically, in the Trou au Natron, the long-term gradual decrease in the P/B ratio reflects a progressive lowering of the lake level. In terms of isotopic signature, the Era Kohor palaeolake record, located in the southern part of Tibesti, generally displayed lower $\delta^{18}O_{diatom}$ values than in the Trou au Natron, located further north. As previously reported by Fontes et al. (1993), this difference might indicate an "altitude effect" since the Emi Koussi/Era Kohor is located at a higher elevation (~3415 m asl) than the Trou au Natron (~2000 m asl).

From ~5500 to 4500 cal yr BP, a negative water balance (E/I > 1) characterized the Tibesti palaeolakes. The highest $\delta^{18}O_{diatom}$ and $\delta^{18}O_{lake}$ values are recorded here and lake water conductivity increased, reflecting evaporative and drier conditions than before. This aridification trend in the Tibesti mountains is consistent with regionally increased aridity, probably induced by the southward retreat of the ITCZ and possibly by the northward retreat of Mediterranean winter humid air masses, causing reduced precipitation in the Tibesti region as seen elsewhere in the Sahara (Gasse, 2000; Hoelzmann et al., 2004; Amaral et al., 2013; Armitage et al., 2015; Tierney et al., 2017; Drake et al., 2018; Cheddadi et al., 2021). Concomitantly, both sites recorded the collapse of formerly dominant planktonic forms while benthic species took over, reflecting low lake levels under evaporative conditions and likely indicating saturated water (Gasse, 1986).

In the period after ~5300 cal yr BP, the final stage of the Trou au Natron record, the highest $\delta^{18}O_{diatom}$ values and water conductivities are inferred from the presence of salt-tolerant species such as *R. gibberula, N. frustulum* and *S. meneghinianus*, however, there is no clear palaeolimnological evidence that Tibesti palaeolakes were saline and/or completely dried out. The range of salinity displayed by the Tibesti high-altitude crater palaeolakes is very low compared to that reported from the current lowland Chadian Sahara lakes (Eggermont et al., 2008; Kröpelin et al., 2008; Van der Meeren et al., 2022). It might be hypothesized that the final stages of Tibesti palaeolakes are either truncated, eroded, or possibly not recorded.

From the early to mid-Holocene (~9500–4500 cal yr BP), the lake water balance (E/I ratio) varied by more than 0.4 between the lowest and the highest values throughout the Tibesti palaeolakes we investigated. This suggests clear long-term reduced water input and/or decreased precipitation amounts. Based on the estimated lake water balance (E/I ratio), we, therefore, attempted a quantitative estimation of inputs (including precipitation). In this study, we assumed that during the AHHP, the air temperature, the relative humidity and the isotopic composition of the atmospheric vapor were constant. Thus, the variation of E/I is assumed to be a function of the variation of I (I = sum of inputs), which in turn varies linearly with P (precipitation). As such, for the Tibesti region, we calculated an average decrease in precipitation amounts of ~35% between ~9300 cal yr BP and ~5000 cal yr BP, which are respectively the peak and the end of the AHHP in our investigated area.

Interestingly, in the Trou au Natron, the $\delta^{18}O_{diatom}$ values and

Fig. 8. Palaeohydrological variations within Tibesti palaeolakes during the AHHP: (a) Planktonic to benthic ratio (P/B) from Trou au Natron (W99 and JK48 sequences) (b) Planktonic to benthic ratio (P/B) from Era Kohor (W566 sequence) (c) Conductivity inferred from transfer function (W99 and JK48 sequences, Trou au Natron) (d) Conductivity inferred from transfer function (W566 sequence, Era Kohor) (e) Lake water isotopic composition estimated from the measured $\delta^{18}O_{diatom}$ (W99 and JK48 sequences) (f) Lake water isotopic composition estimated from the measured $\delta^{18}O_{diatom}$ (W566 sequence) (g) Measured $\delta^{18}O_{diatom}$ (W99 and JK48 sequences) (h) Measured $\delta^{18}O_{diatom}$ (W566 sequence) (i) Lake water balance (E/I ratio) from W99 and JK48 sequences (j) Lake water balance (E/I ratio) from W566 sequence. Vertical dashed black lines depict the main interval of hydroclimate changes in the Tibesti mountains.

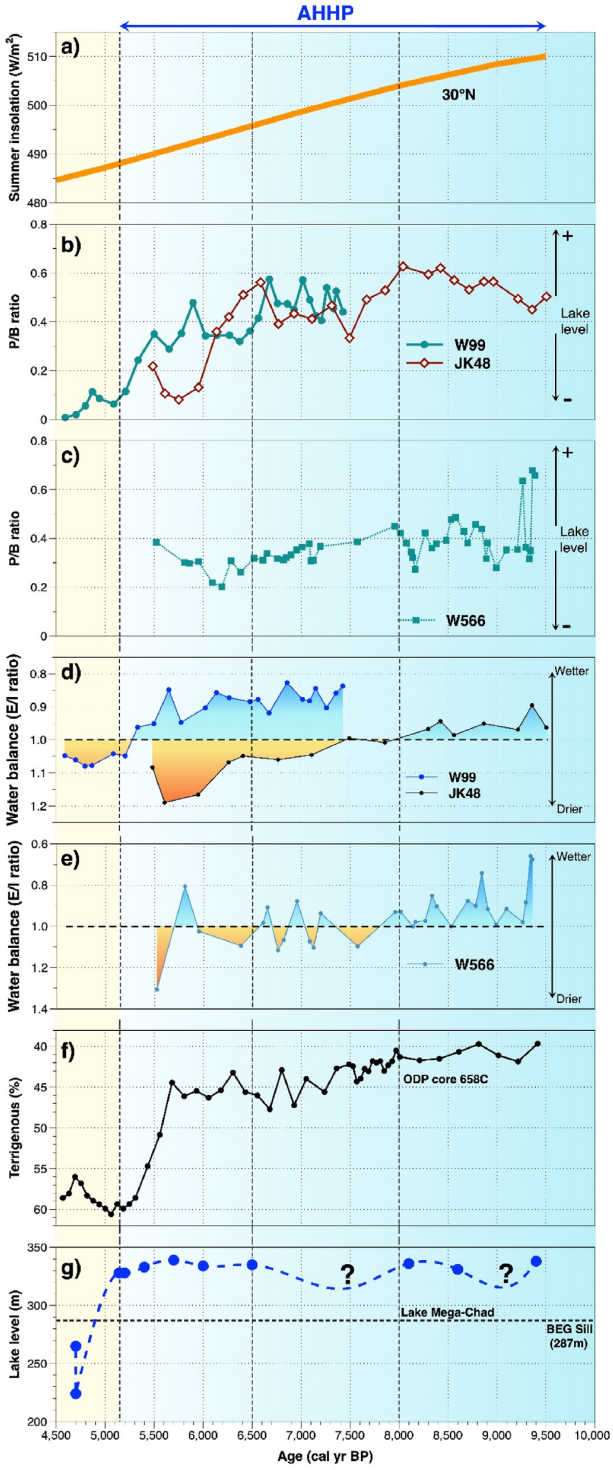

Fig. 9. Comparison of Tibesti records with other hydroclimatic records: (a) The 30°N June insolation, (b) planktonic/benthic diatom ratio (P/B ratio) of Trou au Natron (this study), (c) planktonic/benthic diatom ratio (P/B ratio) of Era Kohor (this study), (d) Lake water balance (E/I ratio) from Trou au Natron (this study), (e) Lake water balance (E/I ratio) from Era Kohor (this study), (f) Terrigenous percentage, ODP 658C (deMenocal et al., 2000), (g) Lake Mega-Chad level fluctuation. The horizontal black dashed line (287 m) represents the elevation of the Bahr El Ghazal (BEG) sill, below which separate lakes exist in the Chad and Bodélé basins (Armitage et al., 2015). Vertical dashed black lines depict the main interval of hydroclimate changes in the Tibesti mountains. The blue vertical bar represents the humidity gradient from the early-to-mid Holocene, and the yellow represents aridity.

reconstructed conductivities of the W99 and JK48 sequences shifted after ~7500 cal yr BP (Fig. 8c and g). The heaviest isotopic signal and the highest conductivities were recorded in the JK48 sequence close to the palaeolake bottom, whereas the lowest values came from the W99 sequence located 330 m higher on the margin of the crater.

When examining the isotope records from a lake, it is imperative to consider the hydrological conditions of the lake and potential changes that could have occurred in the past and could have led to variable and generally high $\delta^{18}O$ values, particularly when investigating crater lakes (Lamb et al., 2000) or in the case of terminal (closed) lakes (Leng and Marshall, 2004). Moreover, it is commonly believed that diagenetic processes, including silica dissolution, can significantly influence a rise in $\delta^{18}O_{diatom}$ values, as previously suggested (Leng and Barker, 2006; Moschen et al., 2006). However, our cleaning procedure of the diatom frustules revealed no evidence of dissolution, showing well-preserved valves as depicted in Fig. 3. Therefore, we can confidently assert that dissolution is not a factor affecting our $\delta^{18}O_{diatom}$ values. Thus, the vertical stratification of the lake water isotopic composition observed in the Trou au Natron palaeolake may be explained by the location of the investigated sedimentary records within the Trou au Natron crater palaeolake. Due to the stratification of the lake, diatoms are limited in their representation to the epilimnion, rather than encompassing the entire water column. Therefore, the JK48 sequence, due to its location near the lake bottom (thereby distant from the shore), records the average composition of the central part of the epilimnion water body, while the W99 sequence records the water inputs to the lake because of its location nearer to the shore area. During the period of aridification after 7500 cal yr BP, the lake experienced reduced precipitation and higher evaporation, which is reflected in the E/I ratio observed in JK48. However, during this time, precipitation had not completely stopped, and inputs to the lake continued to flow down from the shores. The W99 sedimentary record may likely reflect these inputs. This hypothesis is further supported by the fact that JK48 has a more stable composition, while W99 varies considerably, suggesting contrasting responses to inputs depending on their amount. Hence, the isotopic signature captured by JK48 during this period represents the isotopic composition of the entire lake water.

5.2. Hydroclimate evolution of the Tibesti mountains (central Sahara) during the AHHP compared to other regional records

In the Trou au Natron and Era Kohor palaeolakes, fossil diatom assemblages and their oxygen isotope composition provide strong evidence of humid conditions during the early to mid-Holocene, evolving gradually towards arid conditions during the mid-to-late Holocene transition (Fig. 9). The overall trend in the $\delta^{18}O_{diatom}$ records and the diatom assemblages followed the gradual decline in summer insolation at 30°N during the Holocene (Fig. 9a). Our results are consistent with the assumption that during the early to mid-Holocene period, wetter conditions prevailed across the central Sahara due to a strengthened northward extension of the ITCZ and enhanced boreal summer insolation causing the intensification of the African monsoonal rainfall belt (Sun et al., 2019; Chandan and Peltier, 2020; Kutzbach et al., 2020). Moreover, our data support the notion that the timing of the Tibesti palaeolakes' most humid conditions and associated highstand lakes are broadly synchronous with the peak of the AHHP reached in the interval between ~9500 and ~8000 cal yr BP, which is commonly expressed as

a global wet spell over the Sahara and Sahel regions (Gasse, 2000; deMenocal et al., 2000; Lézine et al., 2011; Shanahan et al., 2015; Claussen et al., 2017; Holmes and Hoelzmann, 2017).

Regarding the mid-to-late Holocene period in the Tibesti Mountains, our results provide evidence of a progressive lowering of the lake levels between 6500 and 5000 cal yr BP (Fig. 9b and c). This period is characterized by a decreasing trend in the P/B ratio reflecting the development of benthic diatoms. An increasing trend in $\delta^{18}O_{diatom}$ values suggests an increasingly arid climate which started as early as 6500 cal yr BP. This is strongly supported by pollen data from the Tibesti palaeolakes that indicate the substitution of tropical taxa by desert species (Dinies et al., 2021). The onset of aridity shown by our $\delta^{18}O_{diatom}$ and the estimated water balance (E/I ratio) between 6500 and 5000 cal yr BP corresponds with records from several other lakes indicating a progressive reduction in the moisture balance (Abell and Hoelzmann, 2000) and a transition towards semiarid to arid conditions in the Sahara and Sahel regions (Armitage et al., 2015; Gasse, 2000, 2002; Hoelzmann et al., 2004; Kröpelin et al., 2008; Lézine et al., 2011; Nguetsop et al., 2013). Our proxies characterize this interval as a period of significant changes that might be explained by the progressive southward migration of the ITCZ as a result of declining insolation subsequently leading to a weakened West African summer monsoon (deMenocal, 2015; Dallmeyer et al., 2020). Our findings show a gradual transition from relatively wet to arid conditions, leading to the end of the AHHP after 5300 cal yr BP. As illustrated by the gradual decrease in the P/B ratio (Fig. 9b and c) and the gradually increasing negative water balance, the termination of the AHHP in the Tibesti mountains was progressive and not abrupt as reported elsewhere (deMenocal et al., 2000; Armitage et al., 2015) (Fig. 9f and g). The pronounced drier conditions after ~5300 cal yr BP in the Tibesti were broadly synchronous with those in the Fezzan basin (Lybia) with the final desiccation of palaeolake Shati at ~5300 cal yr BP (Drake et al., 2018).

At a regional scale, our diatom assemblages and $\delta^{18}O_{diatom}$ data clearly demonstrate a period of high rainfall during the AHHP in the Tibesti Mountains, in phase with that of the Central Sahara (Amaral et al., 2013; Cremaschi et al., 2014; Armitage et al., 2015; Drake et al., 2018). As such, our data are coherent with those from Lake Megachad documenting the early to mid-Holocene transition as a period of lake highstand due to high precipitation and increased runoff before abrupt desiccation (Fig. 9g) around ~ 5000 cal yr BP (Armitage et al., 2015). Evidence from slope deposits of the Angamma Delta, located downstream of the Tibesti Mountains, also indicates a lake highstand until ~7500 cal yr BP (Bristow et al., 2018), confirming our positive water balance and inferred freshwater conditions. In addition, in Lake Yoa, located ~400 km to the northeast, pollen data document a major Holocene highstand period with seasonal river flows from the Tibesti region lasting until ~5600 cal yr BP (Kröpelin et al., 2008). Given the geomorphological context of the Tibesti region and the amount of seasonal river flow, it has been suggested that during the AHHP, the Tibesti acted as a water tower and an influent stream to sustain river flows into Lake Yoa (Grenier et al., 2009; Armitage et al., 2015) and Lake Megachad (Bristow et al., 2018).

6. Conclusion

This work provides the first high-resolution account of hydroclimatic variations during the AHHP in the Tibesti Mountains within the Central Sahara. Based on fossil diatom assemblages and their oxygen isotope composition, two distinct lacustrine periods are identified between the early to mid- and the mid-to-late Holocene transitions. From ~9500 to ~6500 cal yr BP, a highstand lake with depleted $\delta^{18}O_{diatom}$ values confirmed by a positive lake water balance (E/I < 1) and low water conductivities coincides with the peak of the AHHP. This reflects effective regional moisture resulting from enhanced precipitation triggered by increased summer insolation. This wet interval is in phase and consistent with the palaeoclimate changes recorded in the adjacent lowlands in the nearby Chadian and Fezzan basins and other sites from the Sahara and Sahel regions in northern Africa.

From ~6500 to 4500 cal yr BP, our results highlight the progressive establishment of arid conditions. High $\delta^{18}O_{diatom}$ values, a negative water balance (E/I > 1), high lake water conductivities and dominant benthic diatoms provide clear evidence of increasing evaporation in the lake catchment and lowering lake levels. The onset of aridification started as early as 6500 cal yr BP and is likely attributed to the gradual decline of summer insolation causing the southward migration of the ITCZ and the weakening of associated monsoonal precipitation. In the Tibesti region, our data showed an average decrease in precipitation amounts of ~35% between the peak and the end of the AHHP. In this area of the central Sahara, the pace of aridification is gradual and the termination of the AHHP is dated between 5500 and 5000 cal yr BP.

Author contributions

F.S., A.N.Y., P.H. and S.K. designed the study. **F.S., P.H. and S.K**. supervised the scientific development of this project. **A.N.Y. and F.S**. provided the diatom data, fossil taxonomy assemblages, oxygen isotope analysis and conductivity inferred values. **S.K**. provided the sedimentary records and pictures from the field. **A.M.** contributed to the geological and palaeoenvironmental background of the Tibesti area. **P.H., M.D. and F.D**. provided lithological sampling, description, chronological data, and topographic profiles with DEM/satellite maps. **J-C.M**. contributed to diatom preparation samples. **C.P**. contributed to taxonomy identification and English revision. **A.A., C.S. and M.C**. contributed to oxygen isotope analysis. **F.C**. contributed to the diatom-based transfer function. **C.V.C** contributed to the lake water modeling experiment. **A.N.Y. and F.S**. prepared the original manuscript and all authors contributed to the discussion of results and commented on the manuscript.

Declaration of competing interest

The authors declare that they have no known competing financial interests or personal relationships that could have appeared to influence the work reported in this paper.

Data availability

Data will be made available on request.

Acknowledgements

This work was supported by a grant from the LEFE/INSU/CNRS program 'COMPILAD' project. This work is part of the PhD thesis research by A.N. Yacoub (Aix-Marseille University) supported by the French Embassy in Chad and the IRD (Institut de Recherche pour le Développement) through the ARTS program. Frank Darius, Michèle Dinies and Philipp Hoelzmann were supported by a grant from the DFG priority program SPP2143 "Entangled Africa" (project number 404354295). Special thanks to Dr Baba Mallaye, Director of the CNRD (Centre National de Recherche pour le Développement), N'Djamena, Chad, for his steady administrative backing and logistic contributions during fieldwork. We thank the anonymous reviewers for their constructive comments. We also thank P. Chaurand, D. Borschneck and Y. Gally for providing assistance with Micro-XRF, XRD and SEM at CEREGE (France).

References

Abell, P.I., Hoelzmann, P., 2000. Holocene palaeoclimates in northwestern Sudan: stable isotope studies on molluscs. Glob. Planet. Change 26, 1–12. https://doi.org/10.1016/S0921-8181(00)00030-8. Paleomonsoon variations and terrestrial environmental change.

Adallal, R., Vallet-Coulomb, C., Vidal, L., Benkaddour, A., Rhoujjati, A., Sonzogni, C., 2019. Modelling lake water and isotope mass balance variations of Lake Azigza in the Moroccan Middle Atlas under Mediterranean climate. Reg. Environ. Change 19, 2697–2709. https://doi.org/10.1007/s10113-019-01566-9.

Alexandre, A., Basile-Doelsch, I., Sonzogni, C., Sylvestre, F., Parron, C., Meunier, J.-D., Colin, F., 2006. Oxygen isotope analyses of fine silica grains using laser-extraction technique: comparison with oxygen isotope data obtained from ion microprobe analyses and application to quartzite and silcrete cement investigation. Geochem. Cosmochim. Acta 70, 2827–2835. https://doi.org/10.1016/j.gca.2006.03.003.

Alexandre, A., Crespin, J., Sylvestre, F., Sonzogni, C., Hilbert, D.W., 2012. The oxygen isotopic composition of phytolith assemblages from tropical rainforest soil tops (Queensland, Australia): validation of a new paleoenvironmental tool. Clim. Past 8, 307–324. https://doi.org/10.5194/cp-8-307-2012.

Amaral, P.G.C., Vincens, A., Guiot, J., Buchet, G., Deschamps, P., Doumnang, J.-C., Sylvestre, F., 2013. Palynological evidence for gradual vegetation and climate changes during the African Humid Period termination at 13°N from a Mega-Lake Chad sedimentary sequence. Clim. Past 9, 223–241. https://doi.org/10.5194/cp-9-223-2013.

Armitage, S.J., Bristow, C.S., Drake, N.A., 2015. West African monsoon dynamics inferred from abrupt fluctuations of Lake Mega-Chad. Proc. Natl. Acad. Sci. USA 112, 8543–8548. https://doi.org/10.1073/pnas.1417655112.

Ball, P.W., White, N.J., Masoud, A., Nixon, S., Hoggard, M.J., Maclennan, J., Stuart, F.M., Oppenheimer, C., Kröpelin, S., 2019. Quantifying asthenospheric and lithospheric controls on mafic magmatism across North Africa. Geochem. Geophys. Geosyst. 20, 3520–3555. https://doi.org/10.1029/2019GC008303.

Bard, E., 2013. Out of the African Humid Period. Science 342, 808–809. https://doi.org/10.1126/science.1246519.

Battarbee, R.W., Jones, V.J., Flower, R.J., Cameron, N.G., Bennion, H., Carvalho, L., Juggins, S., 2001. Diatoms. In: Smol, J.P., Birks, H.J.B., Last, W.M., Bradley, R.S., Alverson, K. (Eds.), Tracking Environmental Change Using Lake Sediments: Terrestrial, Algal, and Siliceous Indicators, Developments in Paleoenvironmental Research. Springer Netherlands, Dordrecht, pp. 155–202. https://doi.org/10.1007/0-306-47668-1_8.

Blaauw, M., Christen, J.A., 2011. Flexible paleoclimate age-depth models using an autoregressive gamma process. Bayesian Anal 6, 457–474. https://doi.org/10.1214/11-BA618.

Bowen, G.J., Wilkinson, B., 2002. Spatial distribution of δ18O in meteoric precipitation. Geology 30, 315–318. https://doi.org/10.1130/0091-7613(2002)030<0315:SDOOIM>2.0.CO;2.

Bristow, C.S., Holmes, J.A., Mattey, D., Salzmann, U., Sloane, H.J., 2018. A late holocene palaeoenvironmental 'snapshot' of the Angamma Delta, Lake Megachad at the end of the African Humid Period. Quat. Sci. Rev. 202, 182–196. https://doi.org/10.1016/j.quascirev.2018.04.025. Archives of Humans, Environments and their Interactions – papers in honour of Professor C. Neil Roberts and Professor Henry F. Lamb.

Broadman, E., Kaufman, D.S., Anderson, R.S., Bogle, S., Ford, M., Fortin, D., Henderson, A.C.G., Lacey, J.H., Leng, M.J., McKay, N.P., Muñoz, S.E., 2022. Reconstructing postglacial hydrologic and environmental change in the eastern Kenai Peninsula lowlands using proxy data and mass balance modeling. Quat. Res. 107, 1–26. https://doi.org/10.1017/qua.2021.75.

Brown, T.A., Farwell, G.W., Grootes, P.M., Schmidt, F.H., 1992. Radiocarbon AMS dating of pollen extracted from peat samples. Radiocarbon 34, 550–556. https://doi.org/10.1017/S0033822200063815.

Brown, S.R., Cartier, R., Schiller, C.M., Zahajská, P., Fritz, S.C., Morgan, L.A., Whitlock, C., Conley, D.J., Lacey, J.H., Leng, M.J., Shanks, W.C.P., 2021. Multi-proxy record of holocene paleoenvironmental conditions from yellowstone lake, Wyoming, USA. Quat. Sci. Rev. 274, 107275. https://doi.org/10.1016/j.quascirev.2021.107275.

Chandan, D., Peltier, W.R., 2020. African Humid Period precipitation sustained by robust vegetation, soil, and Lake feedbacks. Geophys. Res. Lett. 47, e2020GL088728. https://doi.org/10.1029/2020GL088728.

Chapligin, B., Meyer, H., Friedrichsen, H., Marent, A., Sohns, E., Hubberten, H.-W., 2010. A high-performance, safer and semi-automated approach for the δ18O analysis of diatom silica and new methods for removing exchangeable oxygen. Rapid Commun. Mass Spectrom. 24, 2655–2664. https://doi.org/10.1002/rcm.4689.

Chase, B.M., Boom, A., Carr, A.S., Reimer, P.J., 2022. Climate variability along the margin of the southern African monsoon region at the end of the African Humid Period. Quat. Sci. Rev. 291, 107663. https://doi.org/10.1016/j.quascirev.2022.107663.

Cheddadi, R., Carré, M., Nourelbait, M., François, L., Rhoujjati, A., Manay, R., Ochoa, D., Schefuß, E., 2021. Early Holocene greening of the Sahara requires Mediterranean winter rainfall. Proc. Natl. Acad. Sci. USA 118, e2024898118. https://doi.org/10.1073/pnas.2024898118.

Claussen, M., Dallmeyer, A., Bader, J., 2017. Theory and modeling of the African humid period and the green Sahara. In: Oxford Research Encyclopedia of Climate Science. https://doi.org/10.1093/acrefore/9780190228620.013.532.

Collins, J.A., Prange, M., Caley, T., Gimeno, L., Beckmann, B., Mulitza, S., Skonieczny, C., Roche, D., Schefuß, E., 2017. Rapid termination of the African Humid Period triggered by northern high-latitude cooling. Nat. Commun. 8, 1372. https://doi.org/10.1038/s41467-017-01454-y.

Craig, H., Gordon, L., 1965. Deuterium and oxygen 18 variations in the ocean and marine atmosphere. In: Tongiorgi, E. (Ed.), Stable Isotopes in Oceanographic Studies and Paleotemperatures, Spoleto: Conferences in Nuclear Geology.

Cremaschi, M., Zerboni, A., Mercuri, A.M., Olmi, L., Biagetti, S., di Lernia, S., 2014. Takarkori rock shelter (SW Libya): an archive of Holocene climate and environmental changes in the central Sahara. Quat. Sci. Rev. 101, 36–60. https://doi.org/10.1016/j.quascirev.2014.07.004.

Crespin, J., Alexandre, A., Sylvestre, F., Sonzogni, C., Paillès, C., Garreta, V., 2008. IR laser extraction technique applied to oxygen isotope analysis of small biogenic silica samples. Anal. Chem. 80, 2372–2378. https://doi.org/10.1021/ac071475c.

Crespin, J., Sylvestre, F., Alexandre, A., Sonzogni, C., Paillès, C., Perga, M.-E., 2010. Re-examination of the temperature-dependent relationship between δ18Odiatoms and δ18Olake water and implications for paleoclimate inferences. J. Paleolimnol. 44, 547–557. https://doi.org/10.1007/s10933-010-9436-2.

Cui, J., Tian, L., Gibson, J.J., 2018. When to conduct an isotopic survey for lake water balance evaluation in highly seasonal climates. Hydrol. Process. 32, 379–387. https://doi.org/10.1002/hyp.11420.

Dallmeyer, A., Claussen, M., Lorenz, S.J., Shanahan, T., 2020. The end of the African humid period as seen by a transient comprehensive Earth system model simulation of the last 8000 years. Clim. Past 16, 117–140. https://doi.org/10.5194/cp-16-117-2020.

deMenocal, P., Ortiz, J., Guilderson, T., Adkins, J., Sarnthein, M., Baker, L., Yarusinsky, M., 2000. Abrupt onset and termination of the African Humid Period: rapid climate responses to gradual insolation forcing. Quat. Sci. Rev. 19, 347–361. https://doi.org/10.1016/S0277-3791(99)00081-5.

deMenocal, P.B., 2015. End of the African Humid Period. *Nature Geosci* **8**, 86–87 (2015). https://doi.org/10.1038/ngeo2355.

Deniel, C., Vincent, P.M., Beauvilain, A., Gourgaud, A., 2015. The Cenozoic volcanic province of Tibesti (Sahara of Chad): major units, chronology, and structural features. Bull. Volcanol. 77, 74. https://doi.org/10.1007/s00445-015-0955-6.

Dinies, M., Schimmel, L., Hoelzmann, P., Kröpelin, S., Darius, F., Neef, R., 2021. Holocene high-altitude vegetation dynamics on Emi Koussi, Tibesti mountains (Chad, central Sahara). In: Runge, J., Gosling, W.D., Lézine, A.-M., Scott, L. (Eds.), Quaternary Vegetation Dynamics—The African Pollen Database, first ed., pp. 27–50.

Dodd, J.P., Sharp, Z.D., 2010. A laser fluorination method for oxygen isotope analysis of biogenic silica and a new oxygen isotope calibration of modern diatoms in freshwater environments. Geochem. Cosmochim. Acta 74, 1381–1390. https://doi.org/10.1016/j.gca.2009.11.023.

Drake, N.A., Blench, R.M., Armitage, S.J., Bristow, C.S., White, K.H., 2011. Ancient watercourses and biogeography of the Sahara explain the peopling of the desert. Proc. Natl. Acad. Sci. USA 108, 458–462. https://doi.org/10.1073/pnas.1012231108.

Drake, N.A., Lem, R.E., Armitage, S.J., Breeze, P., Francke, J., El-Hawat, A.S., Salem, M.J., Hounslow, M.W., White, K., 2018. Reconstructing palaeoclimate and hydrological fluctuations in the Fezzan Basin (southern Libya) since 130 ka: a catchment-based approach. Quat. Sci. Rev. 200, 376–394. https://doi.org/10.1016/j.quascirev.2018.09.042.

Eggermont, H., Verschuren, D., Fagot, M., Rumes, B., Van Bocxlaer, B., Kröpelin, S., 2008. Aquatic community response in a groundwater-fed desert lake to Holocene desiccation of the Sahara. Quat. Sci. Rev. 27, 2411–2425. https://doi.org/10.1016/j.quascirev.2008.08.028.

Elshaafi, A., Gudmundsson, A., 2021. Central volcanoes and caldera collapses in the late miocene – late pleistocene Tibesti volcanic province, northwest Chad. J. Geodyn. 145, 101846. https://doi.org/10.1016/j.jog.2021.101846.

Fletcher, W.J., Zielhofer, C., Mischke, S., Bryant, C., Xu, X., Fink, D., 2017. AMS radiocarbon dating of pollen concentrates in a karstic lake system. Quat. Geochronol. 39, 112–123. https://doi.org/10.1016/j.quageo.2017.02.006.

Fontes, J.C., Gasse, F., Andrews, J.N., 1993. Climatic conditions of Holocene groundwater recharge in the Sahel zone in Africa. In: Isotope Techniques in the Study of Past and Current Environmental Changes in the Hydrosphere and the Atmosphere. IAEA, Vienna, pp. 231–248. IAEA-SM-329/59.

Gasse, F., 1986. East African Diatoms: Taxonomy, Ecological Distribution. Bibliotheca Diatomologica, Band 11, vol. 201. J. Cramer, Berlin, Germany, p. 44.

Gasse, F., Juggins, S., Khelifa, L.B., 1995. Diatom-based transfer functions for inferring past hydrochemical characteristics of African lakes. Palaeogeogr. Palaeoclimatol. Palaeoecol. 117, 31–54. https://doi.org/10.1016/0031-0182(94)00122-O.

Gasse, F., 2000. Hydrological changes in the African tropics since the last glacial maximum. Quat. Sci. Rev. 19, 189–211. https://doi.org/10.1016/S0277-3791(99)00061-X.

Gasse, F., 2002. Diatom-inferred salinity and carbonate oxygen isotopes in Holocene waterbodies of the Western Sahara and Sahel (Africa). Quat. Sci. Rev. 21, 737–767. https://doi.org/10.1016/S0277-3791(01)00125-1. Interactions between arid and humid records of Quaternary change in drylands (IGCP 413).

Gavrilovic, D., 1969. In: Höevermann, J., Jensch, G., Valentin, H., Woehlke, W., Hagedorn, H., H (Eds.), Klimatabellen für das Tibesti-Gebirge. Arbeitsberichte aus der Forschungsstation Bardai/Tibesti 8, pp. 47–48.

Gèze, B., Hudeley, H., Vincent, P., Wacrenier, Ph., 1959. Les volcans du Tibesti (Sahara du Tchad). Bull. Volcanol. 22, 135–172. https://doi.org/10.1007/BF02596582.

Ghienne, J.-F., Schuster, M., Bernard, A., Duringer, P., Brunet, M., 2002. The Holocene giant Lake Chad revealed by digital elevation models. Quat. Int. 87 (2000),

81–85. https://doi.org/10.1016/S1040-6182(01)00063-5. Holocene Studies, INQUA Commission Meeting, Sevilla.
Gibson, J.J., Edwards, T.W.D., 2002. Regional water balance trends and evaporation-transpiration partitioning from a stable isotope survey of lakes in northern Canada. Global Biogeochem. Cycles 16, 10–11. https://doi.org/10.1029/2001GB001839, 10–14.
Gibson, J.J., Birks, S.J., Yi, Y., 2016. Stable isotope mass balance of lakes: a contemporary perspective. Quat. Sci. Rev., Water Isotope Syst. 131, 316–328. https://doi.org/10.1016/j.quascirev.2015.04.013.
Gonfiantini, R., 1986. Environmental isotopes in lake studies. Environ. Isot. Lake Stud. 2, 113–168.
Gourgaud, A., Vincent, P.M., 2004. Petrology of two continental alkaline intraplate series at Emi Koussi volcano, Tibesti, Chad. J. Volcanol. Geoth. Res. 129, 261–290. https://doi.org/10.1016/S0377-0273(03)00277-4.
Grenier, C., Paillou, P., Maugis, P., 2009. Assessment of Holocene surface hydrological connections for the Ounianga lake catchment zone (Chad). Comptes Rendus Geosci. Histoire climatique des déserts d'Afrique et d'Arabie 341, 770–782. https://doi.org/10.1016/j.crte.2009.03.004.
Guiry, M.D., Guiry, G.M., 2022. AlgaeBase. World-wide electronic publication, National University of Ireland, Galway [WWW Document]. URL. https://www.algaebase.org/about/. accessed September.24.22.
Hély, C., Lézine, A.-M., 2014. Holocene changes in African vegetation: tradeoff between climate and water availability. Clim. Past 10, 681–686. https://doi.org/10.5194/cp-10-681-2014.
Hoelzmann, P., Gasse, F., Dupont, L.M., Salzmann, U., Staubwasser, M., Leuschner, D.C., Sirocko, F., 2004. Palaeoenvironmental changes in the arid and sub arid belt (Sahara-Sahel-Arabian Peninsula) from 150 kyr to present. In: Battarbee, R.W., Gasse, F., Stickley, C.E. (Eds.), Past Climate Variability through Europe and Africa, Developments in Paleoenvironmental Research. Springer Netherlands, Dordrecht, pp. 219–256. https://doi.org/10.1007/978-1-4020-2121-3_12.
Holmes, J.A., 2008. How the Sahara became dry. Science 320, 752–753. https://doi.org/10.1126/science.1158105.
Holmes, J., Hoelzmann, P., 2017. The late pleistocene-holocene African humid period as evident in lakes. In: Oxford Research Encyclopedia of Climate Science. https://doi.org/10.1093/acrefore/9780190228620.013.531.
Global Network of Isotopes in Precipitation (GNIP), 1998. IAEA/WMO [WWW Document]. URL. https://www.iaea.org/services/networks/gnip. accessed September.24.22.
Juggins, S., 2007. C2 Version 1.5: software for ecological and palaeoecological data analysis and visualisation. https://eprints.ncl.ac.uk.
Kostrova, S.S., Biskaborn, B.K., Pestryakova, L.A., Fernandoy, F., Lenz, M.M., Meyer, H., 2021. Climate and environmental changes of the Lateglacial transition and Holocene in northeastern Siberia: evidence from diatom oxygen isotopes and assemblage composition at Lake Emanda. Quat. Sci. Rev. 259, 106905. https://doi.org/10.1016/j.quascirev.2021.106905.
Krammer, K., Lange-Bertalot, H., 1986. Bacillariophyceae. 1. Teil: naviculaceae. In: Ettl, H., Gerloff, J., Heynig, H., Mollenhauer, D. (Eds.), Süßwasserflora von Mitteleuropa, Band 2/1: 1–876. Gustav Fischer Verlag, Stuttgart, Jena.
Krammer, K., Lange-Bertalot, H., 1988. Bacillariophyceae. 2. Teil: bacillariaceae, epithemiceae, surirellaceae. In: Ettl, H., Gerloff, J., Heynig, H., Mollenhauer, D. (Eds.), Süßwasserflora von Mitteleuropa, Band 2/2: 1–596. Gustav Fischer Verlag, Stuttgart, Jena. In: Ettl H., Gerloff J., Heynig H. & Mollenhauer D. (eds) Süßwasserflora von Mitteleuropa, Band 2/2: 1–596. ed.
Krammer, K., Lange-Bertalot, H., 1991a. Bacillariophyceae. 3. Teil: centrales, fragilariaceae, eunotiaceae. In: Ettl, H., Gerloff, J., Heynig, H., Mollenhauer, D. (Eds.), Süßwasserflora von Mitteleuropa, Band 2/3: 1–576. Gustav Fischer Verlag, Stuttgart, Jena.
Krammer, K., Lange-Bertalot, H., 1991b. Bacillariophyceae. 4. Teil: achnanthaceae, Kritische Ergänzungen zu Navicula (Lineolatae) und Gomphonema, Gesamtliteraturverzeichnis Teil 1–4. In: Ettl, H., Gerloff, J., Heynig, H., Mollenhauer, D. (Eds.), Süßwasserflora von Mitteleuropa, Band 2/4: 1–437. Gustav Fischer Verlag, Stuttgart, Jena.
Kröpelin, S., Verschuren, D., Lézine, A.-M., Eggermont, H., Cocquyt, C., Francus, P., Cazet, J.-P., Fagot, M., Rumes, B., Russell, J.M., Darius, F., Conley, D.J., Schuster, M., von Suchodoletz, H., Engstrom, D.R., 2008. Climate-driven ecosystem succession in the Sahara: the past 6000 years. Science 320, 765–768. https://doi.org/10.1126/science.1154913.
Kuper, R., Kröpelin, S., 2006. Climate-controlled holocene occupation in the Sahara: motor of africa's evolution. Science 313, 803–807. https://doi.org/10.1126/science.1130989.
Kutzbach, J.E., Liu, Z., 1997. Response of the African monsoon to orbital forcing and ocean feedbacks in the middle holocene. Science 278, 440–443. https://doi.org/10.1126/science.278.5337.440.
Kutzbach, J.E., Chen, G., Cheng, H., Edwards, R.L., Liu, Z., 2014. Potential role of winter rainfall in explaining increased moisture in the Mediterranean and Middle East during periods of maximum orbitally forced insolation seasonality. Clim. Dynam. 42, 1079–1095. https://doi.org/10.1007/s00382-013-1692-1.
Kutzbach, J.E., Guan, J., He, F., Cohen, A.S., Orland, I.J., Chen, G., 2020. African climate response to orbital and glacial forcing in 140,000-y simulation with implications for early modern human environments. Proc. Natl. Acad. Sci. USA 117, 2255–2264. https://doi.org/10.1073/pnas.1917673117.
Lamb, A.L., Leng, M.J., Lamb, H.F., Mohammed, M.U., 2000. A 9000-year oxygen and carbon isotope record of hydrological change in a small Ethiopian crater lake. Holocene 10, 167–177. https://doi.org/10.1191/095968300677444611.
Leng, M.J., Marshall, J.D., 2004. Palaeoclimate interpretation of stable isotope data from lake sediment archives. Quat. Sci. Rev. 23, 811–831. https://doi.org/10.1016/j.quascirev.2003.06.012. Isotopes in Quaternary Paleoenvironmental reconstruction.
Leng, M.J., Barker, P.A., 2006. A review of the oxygen isotope composition of lacustrine diatom silica for palaeoclimate reconstruction. Earth-Sci. Rev. 75, 5–27. https://doi.org/10.1016/j.earscirev.2005.10.001. ISOtopes in PALaeoenvironmental reconstruction (ISOPAL).
Lézine, A.-M., Hély, C., Grenier, C., Braconnot, P., Krinner, G., 2011. Sahara and Sahel vulnerability to climate changes, lessons from Holocene hydrological data. Quat. Sci. Rev. 30, 3001–3012. https://doi.org/10.1016/j.quascirev.2011.07.006, 2011a.
Maley, J., 2000. Last Glacial Maximum lacustrine and fluviatile Formations in the Tibesti and other Saharan mountains, and large-scale climatic teleconnections linked to the activity of the Subtropical Jet Stream. Glob. Planet. Change 26, 121–136. https://doi.org/10.1016/S0921-8181(00)00039-4. Paleomonsoon variations and terrestrial environmental change.
Manning, K., Timpson, A., 2014. The demographic response to Holocene climate change in the Sahara. Quat. Sci. Rev. 101, 28–35. https://doi.org/10.1016/j.quascirev.2014.07.003.
Ménot, G., Pivot, S., Bouloubassi, I., Davtian, N., Hennekam, R., Bosch, D., Ducassou, E., Bard, E., Migeon, S., Revel, M., 2020. Timing and stepwise transitions of the African Humid Period from geochemical proxies in the Nile deep-sea fan sediments. Quat. Sci. Rev. 228, 106071. https://doi.org/10.1016/j.quascirev.2019.106071.
Moschen, R., Lücke, A., Schleser, G.H., 2005. Sensitivity of biogenic silica oxygen isotopes to changes in surface water temperature and palaeoclimatology. Geophys. Res. Lett. 32. https://doi.org/10.1029/2004GL022167.
Moschen, R., Lücke, A., Parplies, J., Radtke, U., Schleser, G.H., 2006. Transfer and early diagenesis of biogenic silica oxygen isotope signals during settling and sedimentation of diatoms in a temperate freshwater lake (Lake Holzmaar, Germany). Geochem. Cosmochim. Acta 70, 4367–4379. https://doi.org/10.1016/j.gca.2006.07.001.
Nguetsop, V.F., Bentaleb, I., Favier, C., Bietrix, S., Martin, C., Servant-Vildary, S., Servant, M., 2013. A late Holocene palaeoenvironmental record from Lake Tizong, northern Cameroon using diatom and carbon stable isotope analyses. Quat. Sci. Rev. 72, 49–62. https://doi.org/10.1016/j.quascirev.2013.04.005.
Pausata, F.S.R., Gaetani, M., Messori, G., Berg, A., Maia de Souza, D., Sage, R.F., deMenocal, P.B., 2020. The greening of the Sahara: past changes and future implications. One Earth 2, 235–250. https://doi.org/10.1016/j.oneear.2020.03.002.
Permenter, J.L., Oppenheimer, C., 2007. Volcanoes of the Tibesti massif (Chad, northern Africa). Bull. Volcanol. 69, 609–626. https://doi.org/10.1007/s00445-006-0098-x.
Quesada, B., Sylvestre, F., Vimeux, F., Black, J., Paillès, C., Sonzogni, C., Alexandre, A., Blard, P.-H., Tonetto, A., Mazur, J.-C., Bruneton, H., 2015. Impact of Bolivian paleolake evaporation on the δ18O of the Andean glaciers during the last deglaciation (18.5–11.7 ka): diatom-inferred δ18O values and hydro-isotopic modeling. Quat. Sci. Rev. 120, 93–106. https://doi.org/10.1016/j.quascirev.2015.04.022.
Regnéll, J., Everitt, E., 1996. Preparative centrifugation — a new method for preparing pollen concentrates suitable for radiocarbon dating by AMS. Veg. Hist. Archaeobotany 5, 201–205. https://doi.org/10.1007/BF00217497.
Reimer, P.J., Austin, W.E.N., Bard, E., Bayliss, A., Blackwell, P.G., Ramsey, C.B., Butzin, M., Cheng, H., Edwards, R.L., Friedrich, M., Grootes, P.M., Guilderson, T.P., Hajdas, I., Heaton, T.J., Hogg, A.G., Hughen, K.A., Kromer, B., Manning, S.W., Muscheler, R., Palmer, J.G., Pearson, C., Plicht, J. van der, Reimer, R.W., Richards, D.A., Scott, E.M., Southon, J.R., Turney, C.S.M., Wacker, L., Adolphi, F., Büntgen, U., Capano, M., Fahrni, S.M., Fogtmann-Schulz, A., Friedrich, R., Köhler, P., Kudsk, S., Miyake, F., Olsen, J., Reinig, F., Sakamoto, M., Sookdeo, A., Talamo, S., 2020. The IntCal20 northern hemisphere radiocarbon age calibration curve (0–55 cal kBP). Radiocarbon 62, 725–757. https://doi.org/10.1017/RDC.2020.41.
Rirongarti, R., Sylvestre, F., Chalié, F., Paillès, C., Mazur, J.-C., Nour, A.M., Barthelemy, W., Mariot, H., Van der Meeren, T., Poulin, C., Deschamps, P., Abderamane, M., 2022. A diatom-based predictive model for inferring past conductivity in Chadian Sahara lakes. J. Paleolimnol. v. 69 (3), 231–248. https://doi.org/10.1007/s10933-022-00270-9.
Risi, C., Bony, S., Vimeux, F., Jouzel, J., 2010. Water-stable isotopes in the LMDZ4 general circulation model: model evaluation for present-day and past climates and applications to climatic interpretations of tropical isotopic records. J. Geophys. Res. Atmos. 115. https://doi.org/10.1029/2009JD013255.
Roland, N.W., 1974. Zur Entstehung der Trou-Au-Natron-Caldera (Tibesti-Gebirge, Zentral-Sahara) aus photogeologischer Sicht. Geol. Rundsch. 63, 689–707. https://doi.org/10.1007/BF01820838.
Roubeix, V., Chalié, F., 2019. New insights into the termination of the African Humid Period (5.5 ka BP) in central Ethiopia from detailed analysis of a diatom record. J. Paleolimnol. 61, 99–110. https://doi.org/10.1007/s10933-018-0047-7.
Schuster, M., Roquin, C., Duringer, P., Brunet, M., Caugy, M., Fontugne, M., Taïsso Mackaye, H., Vignaud, P., Ghienne, J.-F., 2005. Holocene Lake Mega-Chad palaeoshorelines from space. Quat. Sci. Rev. 24, 1821–1827. https://doi.org/10.1016/j.quascirev.2005.02.001.
Shanahan, T.M., McKay, N.P., Hughen, K.A., Overpeck, J.T., Otto-Bliesner, B., Heil, C.W., King, J., Scholz, C.A., Peck, J., 2015. The time-transgressive termination of the African Humid Period. Nat. Geosci. 8, 140–144. https://doi.org/

10.1038/ngeo2329.
Skonieczny, C., Paillou, P., Bory, A., Bayon, G., Biscara, L., Crosta, X., Eynaud, F., Malaizé, B., Revel, M., Aleman, N., Barusseau, J.-P., Vernet, R., Lopez, S., Grousset, F., 2015. African humid periods triggered the reactivation of a large river system in Western Sahara. Nat. Commun. 6, 1–6. https://doi.org/10.1038/ncomms9751.
Soulié-Märsche, I., Bieda, S., Faure, H., Lafond, R., M'Baidoudji, M., Vincent, P.M., 1995. Radiocarbon dating of a "Characeite" from the crater lake "Trou au Natron", Tibesti, Chad. Terra Nostra, Berlin, p. 258.
Soulié-Märsche, I., Bieda, S., Lafond, R., Maley, J., M'Baitoudji, Vincent, P.M., Faure, H., 2010. Charophytes as bio-indicators for lake level high stand at "Trou au Natron", Tibesti, Chad, during the Late Pleistocene. Glob. Planet. Change 72, 334–340. https://doi.org/10.1016/j.gloplacha.2010.05.004. Quaternary and Global Change: Review and Issues Special issue in memory of Hugues FAURE.
Sun, W., Wang, B., Zhang, Q., Pausata, F.S.R., Chen, D., Lu, G., Yan, M., Ning, L., Liu, J., 2019. Northern hemisphere land monsoon precipitation increased by the green Sahara during middle holocene. Geophys. Res. Lett. 46, 9870–9879. https://doi.org/10.1029/2019GL082116.
ter Braak, C.J.F., Looman, C.W.N., 1986. Weighted averaging, logistic regression and the Gaussian response model. Vegetatio 65, 3–11. https://doi.org/10.1007/BF00032121.
Tierney, J.E., Pausata, F.S.R., deMenocal, P.B., 2017. Rainfall regimes of the green Sahara. Sci. Adv. 3, e1601503. https://doi.org/10.1126/sciadv.1601503.
Vallet-Coulomb, C., Gasse, F., Sonzogni, C., 2008. Seasonal evolution of the isotopic composition of atmospheric water vapour above a tropical lake: deuterium excess and implication for water recycling. Geochem. Cosmochim. Acta 72, 4661–4674. https://doi.org/10.1016/j.gca.2008.06.025.
Van der Meeren, T., Verschuren, D., Sylvestre, F., Nassour, Y.A., Naudts, E.L., Aguilar Ortiz, L.E., Deschamps, P., Tachikawa, K., Bard, E., Schuster, M., Abderamane, M., 2022. A predominantly tropical influence on late Holocene hydroclimate variation in the hyperarid central Sahara. Sci. Adv. 8, eabk1261. https://doi.org/10.1126/sciadv.abk1261.
Vandergoes, M.J., Prior, C.A., 2003. AMS dating of pollen concentrates—a methodological study of late quaternary sediments from south Westland, New Zealand. Radiocarbon 45, 479–491. https://doi.org/10.1017/S0033822200032823.
Vincent, P.M., 1963. Les volcans tertiaires et quaternaires du Tibesti Occidental et central (Sahara du Tchad), Mémoires du BRGM. Bureau de Recherches Géologiques et Minières BRGM, Orléans, p. 307.
Wacrenier P., Hudeley H., Vincent PM., 1958. Notice explicative de la carte géologique provisoire du Borkou-Ennedi-Tibesti au 1:1,000, 000e. Direction des mines et de la géologie AEF, Brazavill, pp.24.
Wolin, J.A., Stone, J.R., 1999. Diatoms as indicators of water-level change in freshwater lakes. In: Stoermer, E.F., Smol, J.P. (Eds.), The Diatoms Applications to the Environmental and Earth Sciences. Cambridge University Press, pp. 174–185.